SAND2019-11536J

The combined effects of hydrogen and aging condition on the deformation and fracture behavior of a precipitation-hardened nickel-base superalloy

Zachary D. Harris[1], Jishnu J. Bhattacharyya[1], Joseph A. Ronevich[2], Sean R. Agnew[1], and James T. Burns[1]*

[1]Department of Materials Science and Engineering, University of Virginia, Charlottesville, VA, USA

[2]Sandia National Laboratories, Livermore, CA, USA

**Corresponding author: zdh8kt@virginia.edu*

Abstract

The effect of hydrogen (H) on the deformation behavior of Monel K-500 in various isothermal heat treatment conditions (non-aged, under-aged, peak-aged, and over-aged) was assessed via uniaxial mechanical testing. H-charged and non-charged specimens were strained to failure to facilitate a comparison of ductility, fracture surface morphology, strength, and work hardening behavior. For all examined heat treatment conditions, H charging leads to a significant reduction in ductility, which is accompanied by a consistent change in fracture surface morphology from ductile microvoid coalescence to brittle intergranular fracture. While H charging led to a systematic enhancement in the yield strength of all heat treatments, the three age-hardened conditions exhibited a more than 2-fold increase relative to the non-aged heat treatment. This suggests that H modifies the dislocation-precipitate interactions, which also manifest themselves through changes in work hardening metrics related to the dislocation storage and recovery rates. In particular, the H-charged peak-aged specimen exhibited a significant increase in initial hardening (dislocation storage) rate relative to the H-charged under-aged specimen. Transmission electron microscopy of these samples confirmed the onset of widespread dislocation looping in the H-charged peak-aged sample, in addition to the planar slip bands characteristic of the non-charged condition. This result suggests that hydrogen induces the particle shearing-to-looping transition at smaller particle sizes. Possible mechanistic explanations for this observed behavior are presented.

Keywords hydrogen embrittlement, Monel K-500, precipitate-dislocation interactions, work hardening

1. Introduction

Hydrogen (H)-induced degradation of structural metals remains a critical failure mode in industries spanning the aerospace, marine, energy, and transportation sectors. However, despite over a century of effort [1], understanding of the microscale processes responsible for this life-limiting effect remains incomplete. Numerous candidate mechanisms have been advanced to describe H-induced degradation, as has been extensively reviewed elsewhere [2–4], with the most commonly cited being: adsorption-induced dislocation emission (AIDE) [5], H-enhanced localized plasticity (HELP) [6], H-enhanced decohesion

(HEDE) [7,8], and H-enhanced vacancy stabilization (HESIV) [9]. Recently, elucidating the role of H on deformation behavior in the context of the aforementioned mechanisms has received extensive attention in the scientific literature [10–16], with the impetus for much of this work being Beachem's observation of small void-like features on the cleavage and intergranular facets in 4300-type steel exposed to 0.6 M NaCl [17]. The presence of these ductile features was subsequently taken as evidence that 'microscopic plasticity' governed H-assisted cracking, which led to the hypothesis that H 'unlocks' dislocations such that they move and/or multiply at lower stresses [17].

This postulation has subsequently been supported by extensive *in-situ* observations of dislocation characteristics under a H atmosphere in an environmental transmission electron microscope (TEM) [3]. Specifically, evidence that H caused enhanced dislocation velocities and reduced dislocation spacing in pile-ups was documented across numerous alloy systems, including Ti, Ni, Fe, 310 stainless steel, 316 stainless steel, Ni_3Al, 7xxx-series aluminum, and IN903 [3]. Additionally, it was suggested that H restricted dislocation cross-slip based on indications that H promoted slip planarity [18]. Mechanistically, this restricted cross-slip was attributed to the combined effects of (1) H-induced reductions in the stacking fault energy (H was estimated to reduce the stacking fault energy by ~20% [19]), and (2) an increased repulsive force between partial dislocations. Considering the latter, Delafosse [20] theoretically demonstrated that H reduces the attraction between edge components in partial dislocations, leading to increased repulsion, larger separation distances between the partial dislocations, and impeded cross-slip. H has also been found to enhance dislocation multiplication. For example, several studies have observed a reduction in the 'pop-in' load of H-charged specimens relative to non-charged specimens during nano-indentation experiments, which were interpreted as a reduction in the energy for homogeneous dislocation nucleation [21–23]. Chen *et al.* reached similar conclusions regarding H effect on dislocation nucleation [24,25]. Specifically, X-ray diffraction (XRD) peak broadening analysis of cold-rolled palladium (Pd) sheets indicated a 6-fold increase in dislocation density for H-charged Pd (0.75 at. % H) relative to non-charged Pd. This observation was qualitatively consistent with TEM analysis showing an increased dislocation density in the rolled H-charged Pd [24], though such XRD results should be interpreted cautiously because the arrangement of the dislocations can induce differences in the apparent dislocation density inferred from peak broadening analysis [26]. While these studies provide insights into the fundamental effects that H has on dislocation processes, attempts to extend this understanding into more complicated, engineering-relevant alloys remain limited. Specifically, though precipitation-hardened alloys are widely employed in structural applications, the effect of H on dislocation-precipitate interactions is largely unexplored [27,28]. Such interactions are acutely pertinent given the well-known sensitivity of H-assisted cracking to bulk slip behavior [29], which can be significantly altered by differences in precipitate morphology.

One common avenue for exploring H effects on deformation behavior is through the comparison of dislocation patterning in the H-charged versus non-charged condition after deformation to a given strain level. For example, Wang *et al.* performed detailed TEM characterization of the deformation structure in pure Ni subjected to high-pressure torsion in the H-charged and non-charged condition [13]. Specimens deformed to equivalent shear strains revealed a reduced average dislocation cell diameter in the H-charged specimens compared to non-charged specimens, suggesting that H accelerates dislocation multiplication (in agreement with the work of Chen *et al.* on Pd [24,25]). However, other studies have shown no statistically significant refinement in the dislocation patterning of H-charged and non-charged Ni [11,30,31]. These contradictory results underscore the challenge of assessing deformation behavior solely through transmission electron microscopy, where the field of interrogation is effectively limited to a few μm^2. Speculatively, the variability in these results could be attributed to heterogeneities in plastic strain and/or variations in grain orientation between compared samples [11,32,33]. As such, assessing dislocation characteristics via a coupled macroscale/microscale approach may yield more consistent insights. One macroscale pathway for assessing variations in bulk deformation behavior is through differences in measured work hardening parameters [34–41]. For example, Cheng *et al.* utilized variations in work hardening data to understand the effect of heat treatment on deformation processes in AA6111 [42]. However, the use of such a framework to understand the effects of H on deformation is very limited [43], especially for precipitation-hardened alloys exposed to H.

The objective of this study is to systematically evaluate the influence of H on the strength, strain hardening, and fracture behavior of Monel K-500 as a function of aging condition. Uniaxial tensile testing was conducted on four isothermal heat treatments (corresponding to the non-aged, under-aged, peak-aged, and over-aged conditions) in the non-charged and H-charged conditions. The results of this testing were then examined in the context of work hardening metrics, coupled with targeted transmission electron microscopy, to provide mechanistic insights into H-induced modifications in dislocation-precipitate interactions.

2. Experimental Methods

2.1. Materials

Monel K-500 is a Ni-Cu superalloy nominally composed of a face-centered cubic (fcc) Ni-Cu solid solution (γ) matrix and a homogenous distribution of highly coherent (<0.1 pct misfit strain), intermetallic γ' ($Ni_3(Al,Ti)$) precipitates [44–47]. The γ' precipitates have an ordered Ll_2 structure, and due to the low misfit and interfacial energy anisotropy, γ and γ' phases form as spherical particles [44]. Two types of carbides have been identified in Monel K-500: (1) a heterogeneous distribution of MC-type carbides (generally TiC) are commonly found in the γ matrix and (2) isolated $M_{23}C_6$-type carbides (where M: Cr,

Mn, Fe, or Ni) have been observed on grain boundaries [44]. Previous reports suggest that the MC-type carbide distribution does not appreciably change under typical aging conditions for Monel K-500 [48] and that their contribution to the strength of Monel K-500 is minimal [44]. Similarly, the $M_{23}C_6$-type carbides are also not expected to significantly impact the mechanical properties of Monel K-500 [44].

All experiments were conducted on a single heat of Monel K-500 procured in the form of a 6-m long, 16-mm diameter bar heat-treated to the solution-annealed condition. The as-received grain structure was nominally equiaxed, with a supplier-reported average grain size of ~10 μm. The bulk composition was evaluated using inductively coupled plasma optical emission spectroscopy (ICP-OES), while glow discharge mass spectroscopy (GDMS) was utilized for trace elemental analysis; the measured composition results are reported in Table 1.

Table 1 – Composition of the tested Monel K-500 heat

Ni	**Cu**	**Al**	**Ti**	**Mn**	**Fe**	**Si**	**Zr**	**P**	**S**	**B**
Weight percent (%)						***Weight part per million (wppm)***				
62.3	31.8	2.96	0.59	0.7	0.78	850	310	69	31	1.2

Specimens for mechanical testing were heat-treated as follows to one of four targeted aging conditions, based on a previously reported age-hardening curves (yield strength vs. isothermal aging time) [49]. Briefly, 38-mm long, 12.7-mm diameter cylindrical blanks were cut from the barstock and then solution-treated in a tube furnace for 1 hour at 1223 K, followed by an immediate water quench; this heat treatment represents the non-aged (NA) condition. Specimens targeted for the under-aged (UA), peak-aged (PA), or over-aged (OA) conditions were then age hardened at 923 K for times of 0.5, 5, or 50 hours, followed by an immediate water quench, respectively. After heat treating, each cylindrical blank was machined into two flat, rectangular tensile specimens with a nominal gage length, width, and thickness of 10.2 mm, 7.1 mm, and 3.2 mm, respectively.

2.2. Hydrogen Charging

Atomic H was introduced into a subset of the tensile specimens *via* gaseous charging; a detailed explanation of the charging procedure is reported elsewhere [50,51]. Briefly, specimens were placed inside an autoclave mounted within a furnace, which was heated to a charging temperature of 573 K and then filled with 99.9999% pure H_2 gas until the target charging pressure of 96.5 MPa was reached. The system was held at these conditions for approximately 144 hours to ensure the development of a uniform H concentration throughout the sample thickness [52]. Upon removal from the furnace, specimens were

immediately stored in a cryogenic freezer maintained at 223 K and then later immersed under liquid nitrogen (LN_2) to minimize H egress prior to mechanical testing.

The lattice H concentration (C_L) can be predicted based on Sievert's Law ($C_L = Sf^{1/2}$; S is the H solubility and f is the H fugacity), where f is determined by the pressure and temperature employed during gaseous charging (*i.e.*, the relationship is material agnostic) [53]. This theoretical framework has been successfully employed for H charging of pure Ni [10,11,50], which offers a useful comparison to the expected C_L in Monel K-500. Using a Ni-30Cu solid solution as a proxy for the matrix phase of Monel K-500, the expected difference in C_L between Ni and Ni-30Cu is expected to be proportional to the change in H solubility. However, reports regarding the solubility of H in a Ni-30Cu solid solution relative to pure Ni are inconsistent. For example, the work of Jones and Pehlke indicates that the H solubility of pure Ni is nominally identical to that of Ni-Cu alloys for <45% Cu by weight [54]; a similar observation was also reported by Ko and McLellan [55]. Conversely, Hagi observed a systematic increase in the H solubility of Ni-30Cu relative to pure Ni, with an approximately 2-fold increase in H solubility measured at the charging temperature employed in this study (573 K) [56]. Moreover, estimates of the H solubility based on measured H permeability and diffusivity values for Monel K-500 suggest a >2-fold increase in solubility relative to pure Ni [57–59]. Based on these historical reports, C_L for Monel K-500 under the employed gaseous charging conditions is estimated to lie between ~70 and ~160 parts per million (ppm), assuming an upper-bound value of 2.25-fold of the solubility of H in pure Ni [50].

To determine the actual H content of the charged specimens, the H concentrations of four 6 x 5 x 2.75 mm pieces from each aging condition were evaluated using an inert gas fusion analyzer at a commercial laboratory (Evans Analytical Group). From these four replicates, average H concentrations of 180, 210, 220, and 220 ppm were measured in the NA, UA, PA, and OA specimens, respectively, which correspond to 1.08 (NA), 1.26 (UA), and 1.32 (PA and OA) atomic (at.) %. Recalling that Sievert's Law only estimates the lattice H concentration [50,53], and therefore, does not account for H trapping at grain boundaries and other microstructural features which may be present (*e.g.* TiC particles), the deviation in C_L for the NA condition (which would most closely approximate a Ni-30Cu solid solution) from the theoretical results is not unexpected [11,50]. Moreover, this increase in C_L over theoretical expectations is also consistent with previous measurements of the diffusible hydrogen concentration ($C_{H,Diff}$), which showed that the tested material heat exhibited a systematically increased $C_{H,Diff}$ relative to five other evaluated heats of Monel K-500 [59–61]. Considering the increased C_L for the aged alloys, this additional H content is likely attributable to H trapping at the γ/γ‘ interface [59,61] (or within the γ‘ precipitate as suggested from simulations by Baskes *et al.* [62]). The variation in C_L between the aged alloys can then be explained by differences in γ’ volume fraction. Specifically, Dey *et al*. demonstrated that the volume fraction of γ’ will

saturate after approximately 2 hours of aging at 923 K. As such, given that the dominant trap site in aged Monel K-500 is the γ' precipitates [59,61], the saturation of the γ' volume fraction would explain the identical H contents measured in the OA and PA heat treatments.

2.3. Mechanical Testing

Uniaxial tensile tests, with the loading direction oriented along the longitudinal axis of the barstock, were performed on a servo-hydraulic load frame operated under actuator displacement control at a constant rate of 0.0041 mm/s, yielding an initial strain rate of ~$4x10^{-4}$ s^{-1}. Each specimen was tested until final fracture, with the specimen elongation actively monitored by an attached extensometer. Prior to straining, H-charged specimens, which had been continually stored under cryogenic temperatures (either in a cryogenic freezer at 223 K or immersed in LN_2), were held at room temperature (RT, ~298 K) for precisely one hour, to allow H to redistribute and reach the equilibrium grain boundary H concentration for this temperature [63]. In addition to the ductility obtained from the employed extensometer, the logarithmic true plastic strain (ε_T) was determined post-test *via* the measured reduction in area (RA); the use of the true plastic strain allows for direct comparison between specimens, including those which exhibited necking [64]. Final area measurements were taken using calibrated optical micrographs of the fracture surface[1], while initial area measurements were made using digital calipers.

The experimental work hardening rate (θ) was determined as follows. The true stress-true strain data was binned and averaged to obtain approximately 200 data points, then these binned true stress-true strain data were numerically differentiated using a 7-point (n = 3) polynomial method adapted from ASTM Standard E647 Appendix XI [65]. The calculated θ vs. ($\sigma_T - \sigma_{YS}$) data, where σ_T is the true stress and σ_{YS} is the 0.2% offset yield strength, was then fit to a sum of two exponential functions: $\theta = ae^{bx} + ce^{dx}$, where x = ($\sigma_T - \sigma_{YS}$). A linear extrapolation was then performed using the fitted θ vs. ($\sigma_T - \sigma_{YS}$) values over the interval of ~100 MPa < ($\sigma_T - \sigma_{YS}$) < 300 MPa to obtain pertinent work hardening metrics (described below), with the lower bound of 100 MPa selected to avoid any influence of the elastoplastic transition region. In addition to the specimens tested to failure, 1-3 specimens from each heat treatment and H-charging condition were deformed to specific targeted strains, where the test was interrupted for a future study. The stress-strain data from these interrupted specimens were included in the analysis to (1) confirm reproducibility of results and (2) improve the rigor of the fit, as shown for the UA/H condition in Figure 1.

[1] Note, due to a combination of necking and slant-type fracture, the RA values determined for the non-charged specimens should be considered an approximation. However, the flat fracture and limited necking observed in the H-charged specimens enabled an accurate measurement of the RA.

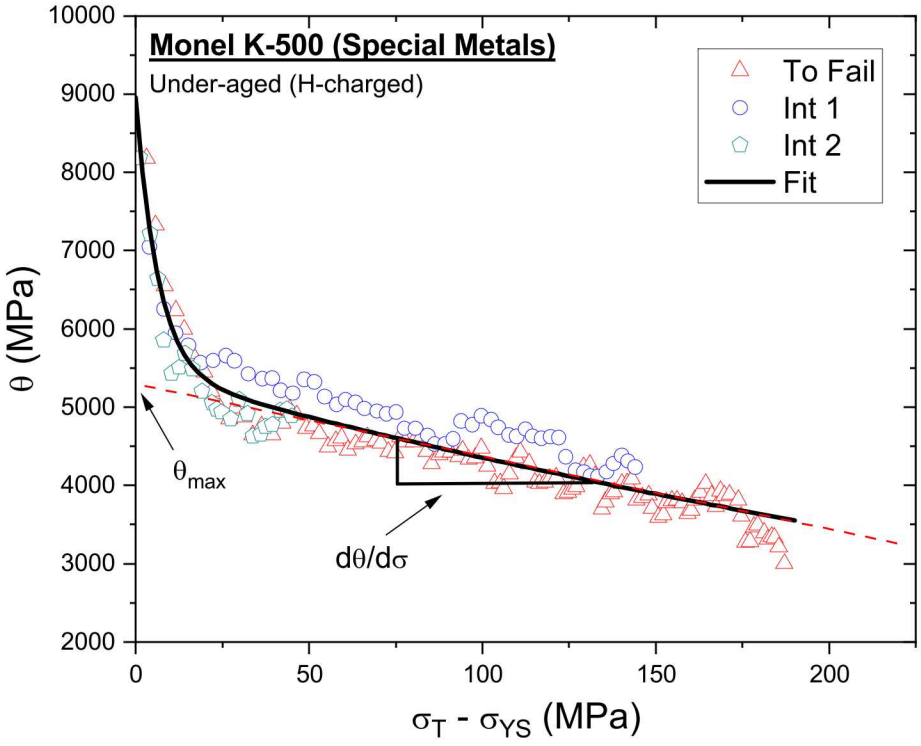

Figure 1 –Plot of the work hardening rate (θ) versus flow stress increase (σ_T - σ_{YS}) illustrating the type of analysis performed for all of the hydrogen (H) charging and aging conditions examined. Note the curve fit of the experimental data as well as the simplification to linearity exhibited beyond the elastoplastic transition, which was used to graphically assess θ_{max} and $d\theta/d\sigma$.

If the strain hardening exhibits linearity on a plot of the θ vs. ($\sigma_T - \sigma_{YS}$), the Voce approximation for Stage III hardening is appropriate, and two parameters may be used to quantitatively compare the work hardening behavior as a function of H and aging condition: the y-intercept (θ_{max}) and the slope ($d\theta/d\sigma$). These metrics are indicative of the rates of dislocation accumulation and recovery, respectively, which can be shown using the Kocks-Mecking model for the evolution of the dislocation density (ρ) with plastic strain [34]:

$$\frac{\partial \rho}{\partial \varepsilon} = \frac{\partial \rho^{+}}{\partial \varepsilon} - \frac{\partial \rho^{-}}{\partial \varepsilon} \approx k_1\sqrt{\rho} - k_2\rho \quad (1)$$

Where $\frac{\partial \rho^{+}}{\partial \varepsilon}$ and $\frac{\partial \rho^{-}}{\partial \varepsilon}$ describe the rates of dislocation accumulation and recovery, which are then dependent on the constants k_1 and k_2, respectively. Note that numerous modifications to this basic framework have been made in the literature to account for the influence of various microstructural features (*e.g.* precipitates, solutes, grain size, free surfaces, etc. [35,37,42]) or the contribution of different populations of dislocation density (*i.e.* forest versus mobile [38,40]). A systematic description of several possible modifications is

presented by Keller and Hug [37], but in general, these modifications are completed through the introduction of additional terms to describe either dislocation storage or recovery. Once the appropriate terms are accounted for, Eqn. 1 can be considered a reasonable description for linking observed macroscale metrics (θ_{max} and $d\theta/d\sigma$) to the rates of dislocation storage and recovery. For example, as shown by Cheng *et al.* for the effect of aging condition on the work hardening behavior of AA6111 [42], θ_{max} and $d\theta/d\sigma$ are directly proportional to k_1 and k_2, respectively, though the relationship between k_1 and θ_{max} is less straightforward compared to k_2 and $d\theta/d\sigma$. Considering the current study, Voce strain hardening is observed as shown by the example presented in Figure 1. However, significant scatter occurs from test-to-test, thereby indicating a need to evaluate the statistical significance of the θ_{max} and $-d\theta/d\sigma$ parameters. Towards this end, the 95% confidence bands were calculated using Matlab and are reported in subsequent sections [66].

2.4. Characterization

The fracture surface morphology for each sample was examined using a Quanta 650 FEG scanning electron microscope (SEM) operated in secondary electron imaging mode with an accelerating voltage between 5-10 keV. Foil specimens for transmission electron microscopy were taken from the gage section of the peak-aged H-charged (PA/H) tensile specimen, with the foil plane parallel to the loading direction. Specimens were prepared as followed: the gage section from the specimen was progressively thinned using SiC papers, finishing at 1200 grit, to a final thickness of 100-110 μm. Care was taken to minimize polishing-induced damage from lower grit sizes by removing at least 3x the maximum particle size of the preceding SiC grinding paper before advancing to next grit size. For example, since the average particle size for the 400-grit SiC paper is ~22 μm, a minimum of 70 μm was removed using the 600-grit paper before advancing to the 800-grit paper. After completion of this grinding procedure, 3-mm diameter discs were punched using a Gatan disc puncher, further thinned to 80-90 μm using a Gatan disc grinder using 1200 grit SiC paper, and then electrochemically polished in a Fischione 110 twin jet polisher using a solution of 60% H_2SO_4 and 40% H_2O (by volume) at ambient temperature (296 to 300 K) with an applied voltage of 5 V. Transmission electron microscopy (TEM) of the obtained specimens was then conducted using an FEI Titan equipped with a double-tilt specimen holder and operated at 300 keV.

3. Results

3.1. Effect of hydrogen on stress-strain behavior and fracture morphology

The true stress-true strain curves for the H-charged and non-charged specimens from each aging condition are shown in Figure 2. Note that the non-charged curves are truncated at the onset of necking, which was assessed using Considere's criterion [67]. Mechanical properties obtained from these tests to

failure are listed in Table 2. Comparison of the flow curves for the H-charged versus non-charged conditions demonstrates that hydrogen degrades the mechanical properties of Monel K-500, regardless of heat treatment condition. First, consistent with previous literature on hydrogen effects in Monel K-500 [68–70], a significant decrease in ductility was observed across all four tested aging conditions in the presence of hydrogen. Second, the fracture stress (approximated by the ultimate tensile strength derived from the engineering stress-strain curve for the non-charged alloys; not shown) was also reduced in the presence of hydrogen by approximately 100 MPa for the NA, UA, and PA conditions, while the OA condition decreased by 60 MPa. Third, the yield strength was found to increase with H-charging across all four aging conditions, with increases on the order of 100 MPa observed in the UA, PA, and OA specimens, while the NA exhibited an increase of 49 MPa.

These differences in ductility between the H-charged and non-charged conditions are consistent with the observed fracture surface morphologies. As shown in Figure 3, each heat treatment displayed evidence of ductile failure *via* microvoid coalescence in the absence of H, in agreement with the results of prior fracture mechanics and slow-strain rate testing of Monel K-500 in laboratory air [60,61,71,72]. The void morphology across the four conditions was qualitatively similar. Considering the fractography of the H-charged samples, shown in Figure 4, each heat treatment exhibited widespread intergranular fracture. As observed in prior studies for hydrogen-charged nickel alloys [10,11,73], slip traces were observed on the intergranular facets for all heat treatment conditions (Figure 5), correlating with the fact that some plastic deformation occurred prior to failure (Figure 2).

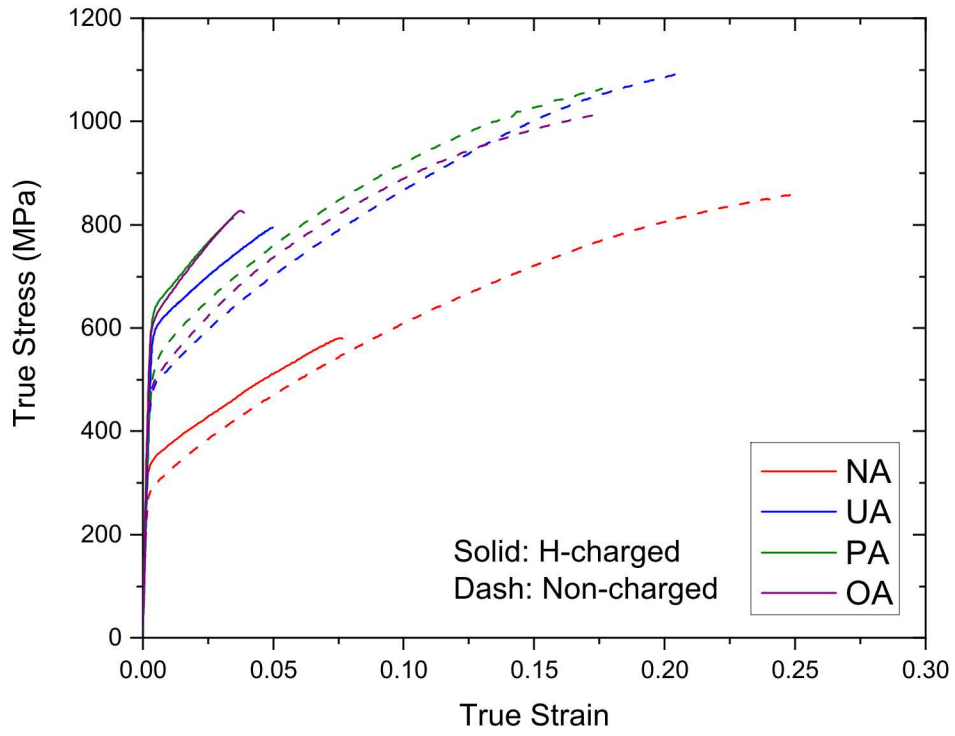

Figure 2 – True stress-true strain curves for the hydrogen (H)-charged and non-charged specimens strained to failure for each heat treatment.

Table 2 – Mechanical properties as a function of heat treatment and hydrogen condition

Testing Condition	Yield Strength (MPa)	Fracture Stress (MPa)	Reduction of Area (%)	True Fracture Strain
NA/H	345	538	8.7	0.091
NA/No H	294	670	50.0	0.693
UA/H	605	757	5.6	0.057
UA/No H	490	890	42.3	0.550
PA/H	641	786	5.5	0.056
PA/No H	526	894	38.1	0.479
OA/H	623	798	4.6	0.047
OA/No H	497	853	39.2	0.497

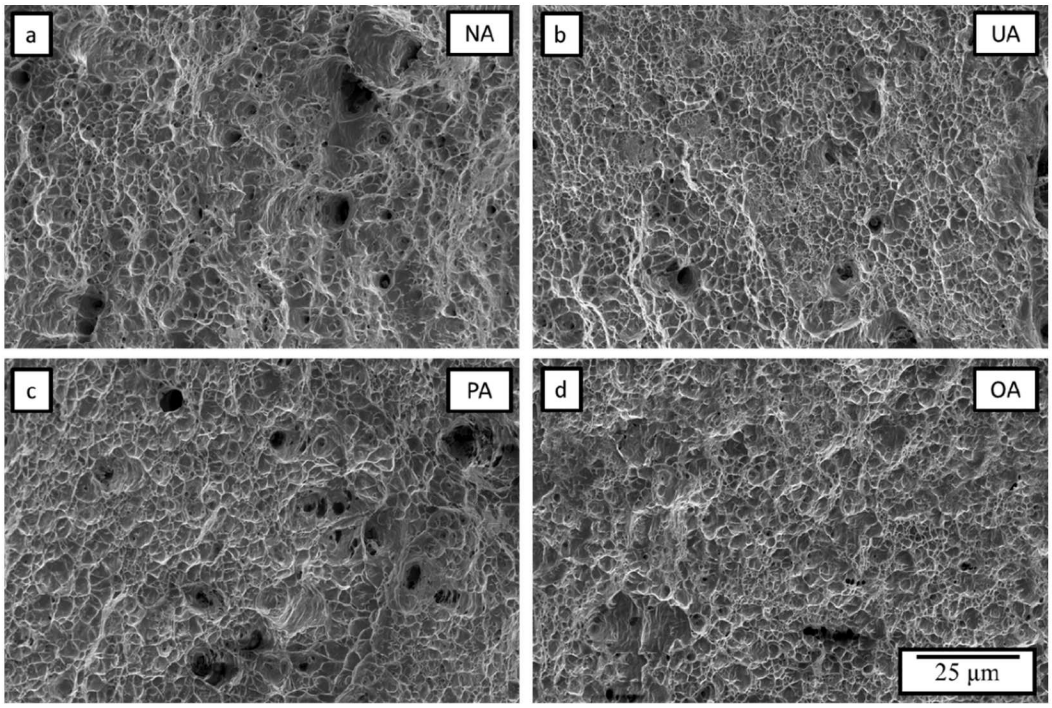

Figure 3 – Fractographs of the (a) non-aged, (b) under-aged, (c) peak-aged, and (d) over-aged heat treatments tested to failure in the non-charged condition.

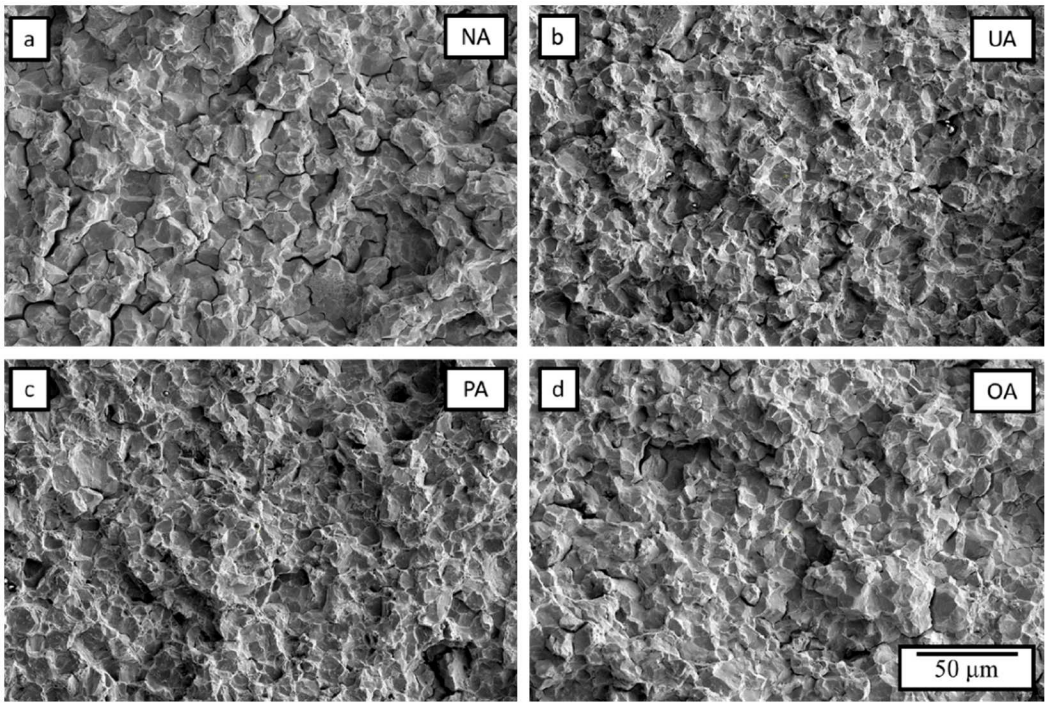

Figure 4 – Fractographs of the (a) non-aged, (b) under-aged, (c) peak-aged, and (d) over-aged heat treatments tested to failure in the hydrogen-charged condition.

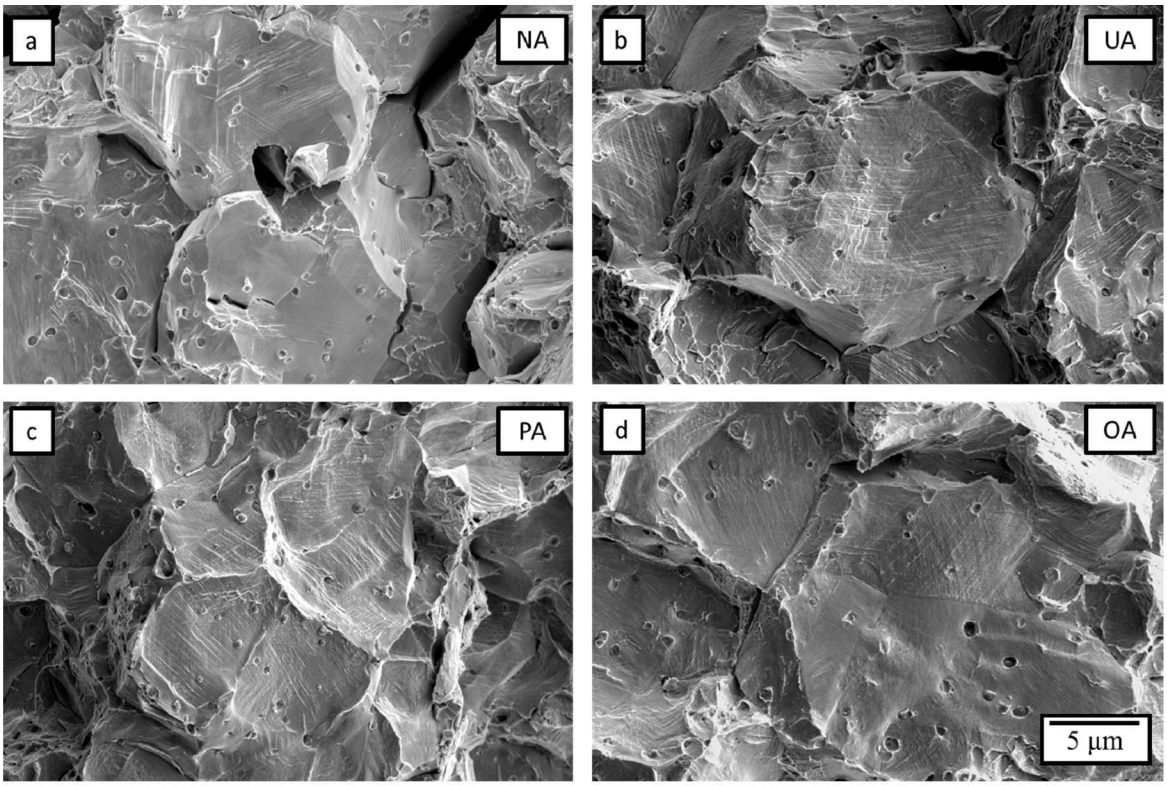

Figure 5 – High-magnification fractographs of the slip traces observed on intergranular facets in the (a) non-aged, (b) under-aged, (c) peak-aged, and (d) over-aged heat treatments tested to failure in the hydrogen-charged condition.

3.2. Effect of hydrogen on work hardening behavior

The work hardening rate (θ) versus flow stress increase ($\sigma_T - \sigma_{YS}$) relationships for the non-charged and H-charged condition in each heat treatment are presented in Figure 6. Each specimen, regardless of H and aging condition, displays an initial rapid decrease in work hardening rate at small ($\sigma_T - \sigma_{YS}$), which is related to the significant changes in slope within the elastoplastic transition of the true stress-true strain curve [42]. Beyond this transition region, each of the specimens (regardless of H content) exhibits an essentially linear decrease in the work hardening rate with increasing ($\sigma_T - \sigma_{YS}$). Clear variations in the character of this linear region arise among the tested specimens, both as a function of heat treatment and as a function of H, which can be described by θ_{max} and $-d\theta/d\sigma$. These metrics were determined from the work hardening data for each H/heat treatment combination as defined in Figure 1 and then plotted in Figure 7, along with the error bars derived from the calculated confidence bands for each testing condition. Figure 7a reveals a distinct effect of H on the evolution in dislocation storage rate (indicated to the first-order by the determined θ_{max} values [42]) with heat treatment. While the NA and UA heat treatments exhibit similar θ_{max} values in the charged and non-charged condition (note that differences in θ_{max} < 300-400 MPa are not generally considered significant [74]), a clear increase in θ_{max} ~1500 MPa was observed for the H-charged

PA and OA conditions relative to the respective non-charged results. Figure 7b shows that H also influences the dislocation recovery rates, as demonstrated by changes in $-d\theta/d\sigma$. Considering the non-charged condition, similar values of $-d\theta/d\sigma$ ($\approx$6) were observed for NA/No H and UA/No H, followed by an increase to 8.1 and 10.6 for the PA/No H and OA/No H heat treatments, respectively. Conversely, upon adding H, $-d\theta/d\sigma$ was found to be increased for all heat treatments relative to the non-charged condition, with the exception of OA, which had a similar $-d\theta/d\sigma \approx 10.7$ for both conditions. In particular, $-d\theta/d\sigma$ were elevated for the H-charged UA and PA samples, compared to their respective non-charged condition results.

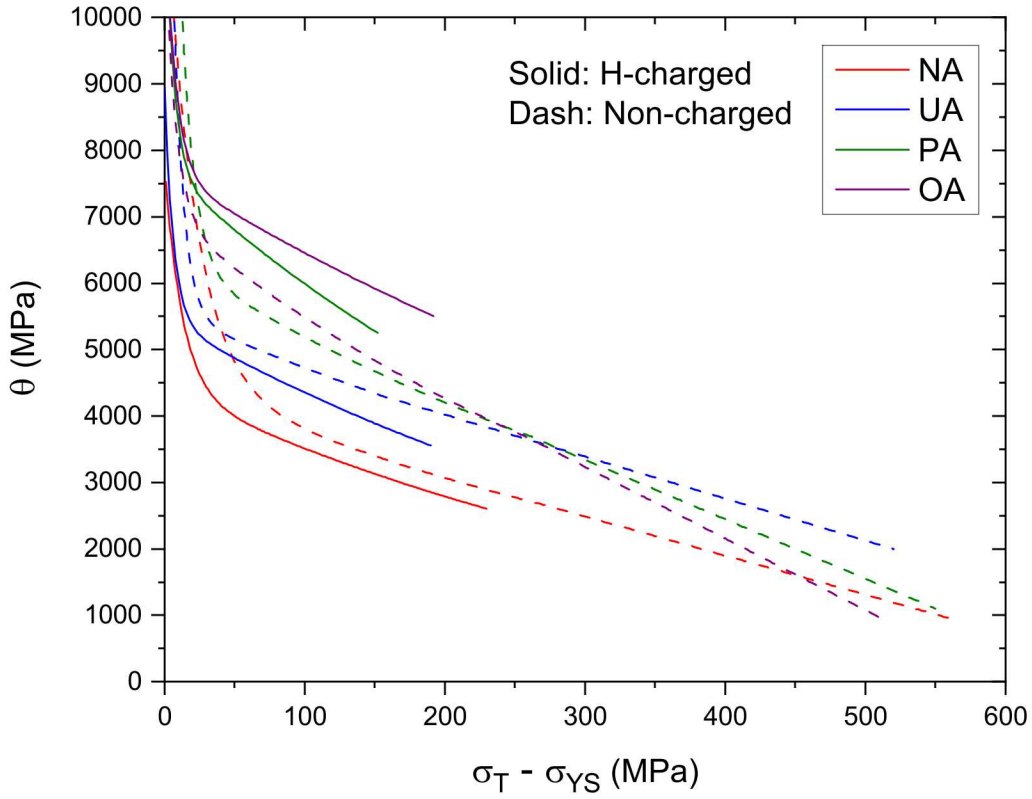

Figure 6 – Work hardening rate versus flow stress increase for the hydrogen (H)-charged and non-charged specimens strained to failure for each heat treatment.

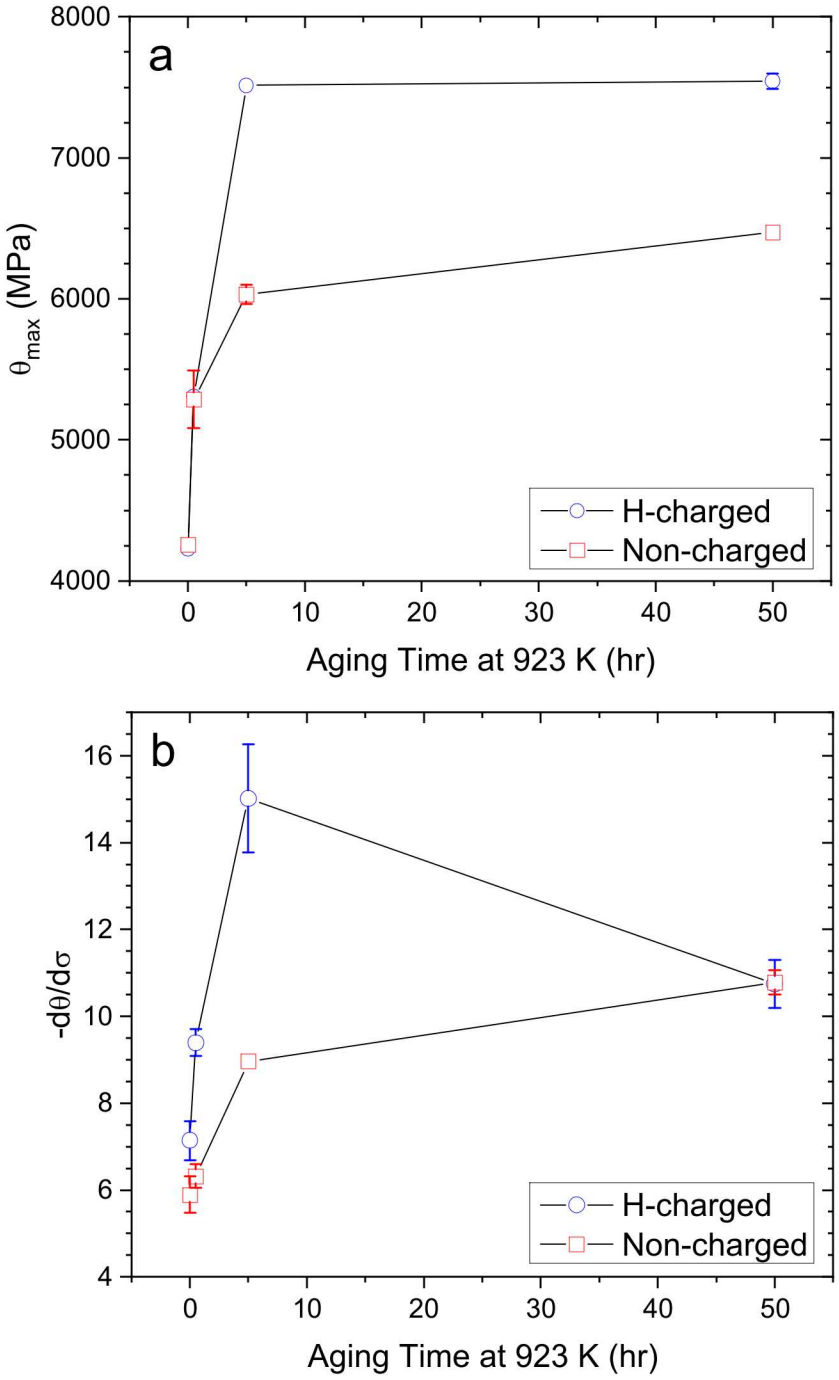

297

298 *Figure 7 – Plot of (a) θ_{max} and (b) $-d\theta/d\sigma$ as a function of aging time and hydrogen (H). Parameters were*
299 *obtained using the graphical method shown in Figure 1, with error bars defined based upon a linear fit to*
300 *the bounds of the confidence bands for each heat treatment/hydrogen content combination. Note that the*
301 *error bars were removed for plot clarity if they fell within the width of the respective data symbol.*

302

3.3. Verification of similar precipitate morphologies between the non-charged and H-charged conditions

A critical assumption of the current work is that the γ' morphology (*e.g.* size) and distribution is not appreciably modified during the thermal charging procedure (at 573 K) utilized to introduce hydrogen into the tensile specimens. As discussed by Cheng et al. [42], variations in precipitate size can induce changes in the work hardening behavior, which would then complicate direct assessment of the role of H for a given heat treatment condition. The extrapolation of γ' coarsening kinetics data previously obtained for Monel K-500 [44] suggests that negligible growth (<0.01 nm) should be expected after 150 hours at 573 K. However, while limited growth is expected in the age-hardened alloys based on these calculations, the extended time at elevated temperature could be sufficient to enable the nucleation of γ' in the NA heat treatment. To assess this possibility, a 12.7-mm diameter, 2-mm thick disc specimen in the NA condition was aged at 573K for 335 hours, then immediately water quenched. Ten Rockwell B (HRB) hardness measurements were taken from polished samples in the (1) baseline NA condition, and (2) the 573K annealed NA condition, which yielded an average hardness of 83.3 ± 2.7 and 82.8 ± 2.1 HRB, respectively. These similarities in measured hardness suggest that γ' nucleation would not occur due to the extended time at 573 K, which is significant given that the NA condition will have the highest driving force for change in the precipitate microstructure.

In addition to the effect of prolonged exposure to elevated temperatures on the precipitate morphology, it has previously been shown that H can stabilize the vacancy concentration above that predicted by thermodynamics [10,15], which may cause an acceleration in coarsening kinetics or assist in the nucleation of precipitates in the NA condition. Regarding the latter, an increase of ~50 MPa in yield strength (see Table 2) is observed for the NA sample, after H-charging, which could be attributed to the nucleation of γ'. However, a similar increase in yield strength was observed for 304 stainless steel charged with ~1 at. % H [75], suggesting that the observed increase may be due to solute strengthening effects and not the nucleation of γ' precipitates. To assess the possibility of H-enhanced particle coarsening of the aged heat treatments during the H charging process at 573 K, an assessment of the precipitate size distribution was completed using transmission electron microscopy on foil specimens prepared from the PA/H tensile specimen. To ensure a representative evaluation of the γ' size, a total of 375 precipitates were examined from multiple locations on two separate foil specimens prepared from the PA/H tensile specimen. This measured γ' size distribution was then compared to a distribution measured for the PA/No H condition in prior work [49]; the distribution for OA/No H was also included for comparison. As shown by Figure 8, the distributions for the non-charged and hydrogen-charged PA specimens are nominally identical, with the difference in the average particle radius between the two conditions within the calculated 95% confidence

interval. Additionally, clear differences are observed between the two PA conditions and the OA/No H specimen, with the latter exhibiting a ~2-fold increase in the average particle size and a significantly wider distribution of observed particle sizes, as indicated by the ~2-fold increase in the 95% confidence interval.

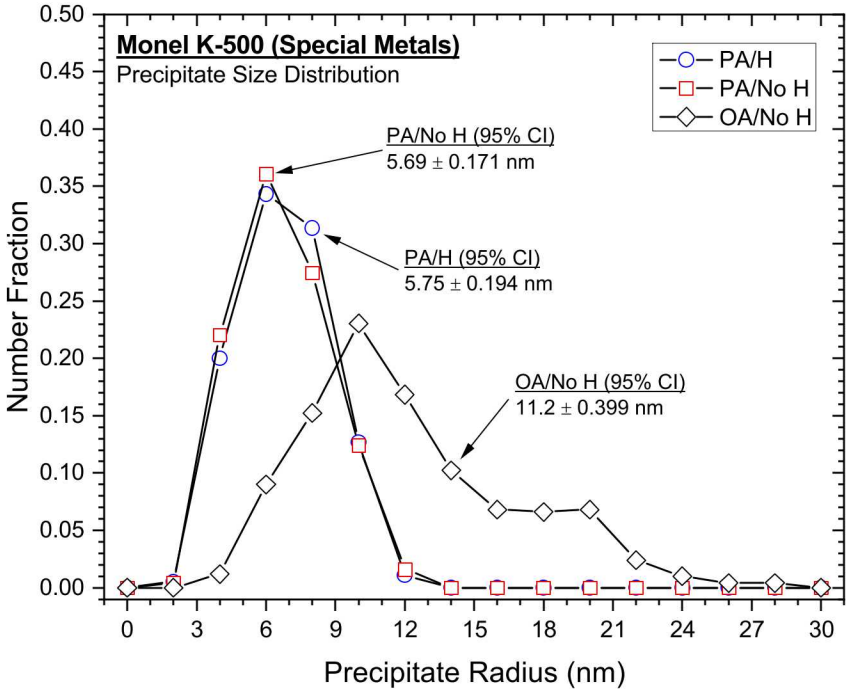

Figure 8 – Comparison of the γ' size distribution for the non-charged over-aged condition (OA/No H) and both the non-charged (PA/No H) and hydrogen-charged (PA/H) peak-aged conditions, along with the average and 95% confidence interval of the precipitate size for each condition.

4. Discussion

The presented flow curves (Figure 2) demonstrate that the ductility and fracture stress (Table 2) of Monel K-500 are decreased in the presence of H across all four tested aging conditions. Fractography corroborated this assessment based on a systematic transition in fracture morphology from ductile microvoid coalescence to intergranular failure for all H-charged specimens (Figures 3-5). Analysis of work hardening data (Figure 6) revealed a clear effect of H on the deformation behavior of Monel K-500, as quantified by θ_{max} and $-d\theta/d\sigma$ (Figure 7). In particular, systematic increases in θ_{max} and $-d\theta/d\sigma$ were observed for the PA/H relative to PA/No H. Lastly, examination of the precipitate size distribution for PA/H and PA/No H conditions indicates that the H charging procedure did not induce statistically significant differences in the precipitate morphology (Figure 8). Based on these observations, the following discussion will: (1) assess the role of H on the mechanical behavior of Monel K-500 as a function of aging condition and (2) comment on the mechanistic implications of the presented results as well as identify research questions for future study.

4.1. Effect of hydrogen on the mechanical behavior of Monel K-500 as a function of aging condition

4.1.1 Effect of hydrogen on yield strength

Comparison of the *change* in yield strength due to H-charging indicates a systematic difference between the NA condition and the three age-hardened heat treatments (Figure 2, Table 2). Specifically, a difference in yield strength of 51 MPa was observed for NA, while increases of greater than 115 MPa were observed for UA, PA, and OA. The precipitate size distributions and analysis presented in Section 3.3 demonstrates that it is unlikely that this increase is caused by modification of the precipitates during the elevated temperature gaseous charging procedure, suggesting that H is responsible for the observed increase in yield strength. It is useful then to consider how H may impact the operative strengthening mechanisms for each aging condition. As shown in Eqn. 2, the yield strength can be represented as the sum of the contributions from each potential strengthening mechanism: lattice friction (σ_0), cold work (σ_D), grain size (σ_{GB}), precipitation hardening (σ_{PH}), and solid solution strengthening (σ_{ss}).

$$\sigma_{YS} = \sigma_0 + \sigma_D + \sigma_{GB} + \sigma_{PH} + \sigma_{ss} \quad (2)$$

For the NA condition, the effect of H on precipitation hardening and cold work can be reasonably considered negligible given that (1) precipitates are not present in the NA heat treatment, and (2) the specimens were received in the annealed condition from the supplier, re-solutionized at 1223 K and quenched, and then effectively annealed again during the H charging process (which was completed at 573 K). Similarly, it is unlikely that an effect of H on the lattice resistance is responsible since σ_0 is a small contributor to the strength of fcc alloys and any subtle effect of H on the lattice resistance can be subsumed into the solid solution strengthening term (σ_{ss}).

The effectiveness of grain size strengthening could be modified by H-charging in two ways. First, it is possible that the strength could be reduced by grain growth that could have occurred during the H charging. However, prior work on the same heat of Monel K-500 demonstrated negligible grain growth after 50 hours at 923 K [49], where the driving force for grain growth would be much higher than the H charging temperature employed herein (573 K) [76,77]. Second, H could affect the difficulty of grain boundary transmission by dislocations (*i.e.* increase the locking constant of the Hall-Petch relationship [78]), thereby increasing the contribution of a given grain size to the yield strength. Such an effect has been documented for carbon in steel, though the efficacy appears to depend on the solute, as nitrogen was found to have minimal influence on grain boundary strengthening [79,80]. Considering H, reports are inconsistent and predominantly conducted in Fe-based alloys. For example, Mine *et al*. found no change for metastable austenitic stainless steels [81], while Bernstein reported no influence in Fe-0.15Ti, but did note an increase

for decarburized Fe [82]. Similarly, Caskey observed a systematic increase in the locking constant for H-charged 304L [83]. In the case of pure Ni, Wilcox and Smith found negligible difference in the grain size-dependent yield strength with H exposure [84], while the data of Lawrence *et al.* suggests a slight increase in the locking constant for H-charged Ni (albeit on a sample size of two different grain sizes) [10]. Based on these reports, H may modify the efficacy of grain size strengthening, but not at a sufficient level to fully account for the observed increase in yield strength for the NA condition. Such a conclusion is consistent with the findings of a recent literature review on the Hall-Petch effect [78], which attributed most of the strength contribution from interstitials in Nb to solid solution hardening as opposed to modifications in the efficacy of grain size strengthening. As such, H-induced solid solution strengthening is likely the dominant contributor to the 51 MPa increase observed in the NA condition upon H charging.

Interestingly, the age-hardened specimens all exhibited a >2-fold increase in yield strength compared to the NA condition (Table 2). As the arguments for the lack of H effects on the lattice friction, cold work, and grain size contributions to yield strength set forth for the NA condition are also pertinent to the aged conditions, such factors would not explain this additional increase. This suggests that the increase in strength for these age-hardened alloys is due to either (1) additional H-induced increases in the solid solution strengthening relative to the NA condition or (2) an effect of H on precipitate strengthening mechanisms. Regarding the former, though the aged samples contained roughly 20% more H than the NA sample, empirically-based estimates and theoretical calculations (shown in Figure 9) suggest that the increased solid solution strengthening associated with this added H content does not explain the observed increase in yield strength for these alloys as compared to the NA condition. For example, Ulmer and Altstetter conducted a systematic evaluation of the increase in yield strength of single phase, H-charged 304 stainless steel, which revealed a linear dependence on the yield strength with increasing H concentration where the yield strength increased by 40-50 MPa/at. % of H up to 10 at. % [75]. Assuming a similar linear approximation based on the increase in yield strength for the NA condition (shown by the dashed line in Figure 9), an increase on the order of 60-65 MPa would be expected between the H-charged and non-charged conditions for the UA, PA, and OA heat treatments. Considering theoretical predictions, while more rigorous models for solute strengthening (both analytical [85–87] and computational [16,88–90]) exist for solid solution strengthening, the Mott model [86] can be employed as a first-order assessment, as demonstrated by Nakada *et al.* for the effect of nitrogen and carbon on the yield strength of Fe [91]:

$$\Delta\sigma_{YS} = \frac{1}{2} M \mu \epsilon^{\frac{4}{3}} f \left[\frac{f^{\frac{2}{3}} (\log f)^4}{0.5} \right]^{\frac{1}{3}} \quad (3)$$

Where M is the Taylor factor for an fcc material, μ is the shear modulus (taken to be 72 GPa based on a Ni-30Cu matrix [92]), f is the atom fraction of solute, and ϵ is the misfit strain defined by:

$$\epsilon = \frac{1}{a}\frac{da}{df} \tag{4}$$

Where a is the lattice parameter and $\frac{da}{df}$ represents the change in lattice parameter with solute concentration. Using the data of Baranowski *et al.* [93] for pure Ni, and assuming weak coupling between the interstitial H and substitutional Cu solute (*i.e.* Baranoswki's relation for Ni-H holds for Ni-Cu-H), $\frac{da}{df}$ can be calculated as ~0.3 Å/unit concentration and the lattice parameter can be approximated as that of uncharged Ni-30Cu based on the work of Sakamoto (a = 3.55 Å) [58]. As shown by the dotted-dashed line in Figure 9, the prediction of Mott's simple model is in reasonable agreement with the empirical estimate based on the results of Ulmer and Altstetter [75]. Critically, this analysis also suggests that the increased magnitude of strengthening observed for the H-charged aged conditions is not attributable to solid solution effects, thereby suggesting an H-induced modification of dislocation-precipitate interactions.

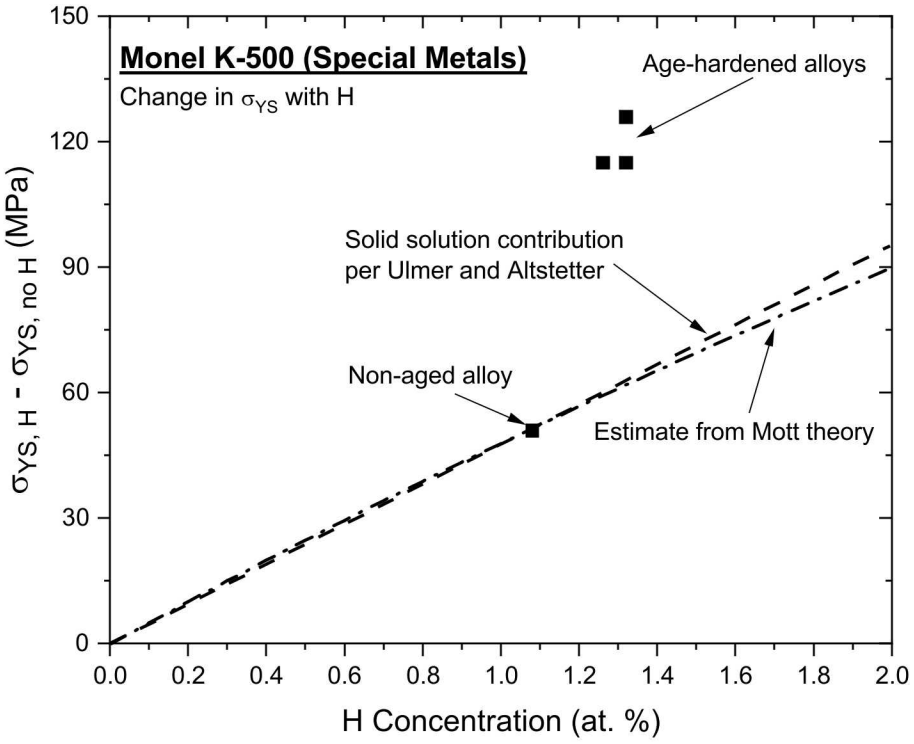

Figure 9 - Observed increase in yield strength versus hydrogen concentration. Note that the dashed line is adapted based on the work of Ulmer and Altstetter [75] *and the dotted line is the prediction based on Equation 4.*

4.1.2. Effect of hydrogen on the initial hardening rate (θ_{max})

Previous studies regarding the sensitivity of θ_{max} to the presence of solute atoms suggest either a limited influence of solute [34,42] or the sensitivity being dependent on alloy/solute combination [94]. Based on the results in Figure 7a, θ_{max} appears to be independent of H-charging in the NA and UA alloys, while large increases in θ_{max} were observed for the PA and OA conditions. Historically, such increases in the work hardening rate for different aging conditions in alloys hardened by secondary phases are generally attributed to two factors: (1) image stresses from concentric dislocation loops that form around precipitates (*i.e.* looping processes) [95,96] and/or (2) constraint effects when particles no longer co-deform with the matrix (*i.e.* load partitioning) [42,95,97]. Particles which no-longer co-deform then contribute to the work hardening rate *via* elastic constraint (due to the mismatch in accommodated plastic strain between the matrix and precipitate), with the magnitude of this effect being proportional to βGf [95], where β is a scaling factor on the order of 0.5 to account for precipitate shape *via* Eshelbian micromechanics, G is the shear modulus of the particle, and f is the particle volume fraction. However, it is important to recognize that these looping and load partitioning contributions are not mutually exclusive, as the onset of particle bypassing inherently induces non-uniform load accommodation between the matrix and precipitate phases. This notion of a coupled effect on the work hardening rate is supported by neutron diffraction experiments on Ni-base superalloys during deformation [98–100]. For example, modeling by Francis *et al.* of the phase-specific (γ and γ') deformation based on neutron diffraction measurements on RR1000 with varying sizes of γ' revealed that the hardening rate of the γ matrix increased as the γ' size increased [98]. As such, though Francis *et al.* demonstrate that load partitioning is the dominant contribution to work hardening in RR1000 [98], this need for an increased hardening rate in the matrix phase in order to capture the deformation behavior of the aggregate material ($\gamma + \gamma$') implies that both load partitioning and looping-associated back-stresses (to an unknown degree) are operative in γ'-strengthened alloys.

It is useful then to consider both possible contributions to work hardening in order to understand the observed variation in θ_{max} for the evaluated heat treatments and H contents. Given a shear modulus of 77 GPa for Ni_3Al [101] and a maximum γ' volume fraction of 6.5% [44], the largest work hardening contribution from load partitioning for Monel K-500 can be estimated as ~2500 MPa, assuming the entire volume fraction of γ' is no longer co-deforming [95,97]. Regarding the non-charged alloys, prior work on Monel K-500 demonstrates that the transition from particle cutting to bypassing occurs at an aging time between the current PA and OA heat treatments [46,49]. As such, looping-associated back-stresses are not expected to contribute to θ_{max} until the OA condition, since shearable particles have minimal effect on θ_{max} [35,42]. Given that several authors have reported load partitioning for even 'fine' γ'-containing Ni-base superalloys [98–100], which exhibit particle shearing, it is reasonable to suggest that the observed ~1000

MPa increase in θ_{max} from the NA/No H to UA/No H condition is likely due to load partitioning effects. Similarly, the increase in θ_{max} of ~700 MPa between the UA/No H and PA/No H is also assumed to be due to load partitioning, with this additional increase arising from a larger volume fraction of particles that do not co-deform. Lastly, considering the increase in θ_{max} of ~500 MPa between the PA/No H and OA/No H, the prior observation of dislocation loops in the OA/No H condition [49] suggests that both possible contributions to work hardening may be active. Based on the work of Francis *et al.* [98] it is speculated that this 500 MPa increase is principally due to load partitioning effects, however it is likely there is a tangible contribution of looping-induced back-stresses. Regarding the H-charged alloys, the increase of ~1000 MPa in θ_{max} between the NA/H and UA/H conditions can likely be attributed to load partitioning effects, given the similarities with the non-charged condition. However, θ_{max} is then found to strongly increase by ~2250 MPa between the UA/H and PA/H conditions. This increase of ~3250 MPa over the NA/H condition is larger than the maximum contribution predicted for load partitioning effects (~2500 MPa), which implies that H-charging has induced an early transition to bypassing mechanisms (in order to generate the looping-induced back-stresses). Interestingly, θ_{max} was found to be similar for the PA/H and OA/H conditions; speculatively, this result may indicate that a saturation of the looping contribution to work hardening has occurred.

Based on the discussion above, the most tractable mechanistic explanation for the increased work hardening rate (as quantified by θ_{max}) between the PA/H and PA/No H conditions is that H induces the transition from particle shearing to bypassing at smaller precipitate sizes. This hypothesis is supported by (TEM) of the bulk slip morphology in a PA/No H specimen compressively deformed to 2% plastic strain in prior work [49] and the PA/H specimen strained to failure, shown in Figures 10 and 11, respectively. Specifically, the PA/No H specimen exhibits large planar arrays with evidence of dislocation coupling (highlighted by the red arrows in Figures 10b and 10d), with limited evidence of dislocation bypassing. Conversely, while the PA/H specimen contained planar bands (red arrows in Figure 11a) oriented along the trace of a {111} plane, particle bypassing was also observed (*e.g.* dislocation loops indicated by the red arrows in Figure 11c-d). Alternate explanations for the observed dislocation loops are not compelling, but include changes in particle size distribution between PA/No H and PA/H or the injection of dislocation loops during the TEM analysis. Specifically, the particle size distributions plotted in Figure 8 demonstrate that the average precipitate size between PA/No H and PA/H is sufficiently similar to suggest that modifications in precipitate size are not responsible. Similarly, the possibility that the dislocation loops were injected by the TEM is unlikely as dislocation loops in Ni alloys generally require long exposure times and/or accelerating voltages on the order of 1 MeV [102]. As such, it is concluded that H acts to decrease the precipitate size required for the onset of particle bypassing mechanisms. However, *why* H induces a

transition from dislocation shearing to bypassing of the precipitates at an earlier stage of age hardening will be explored in the following discussion on dislocation recovery.

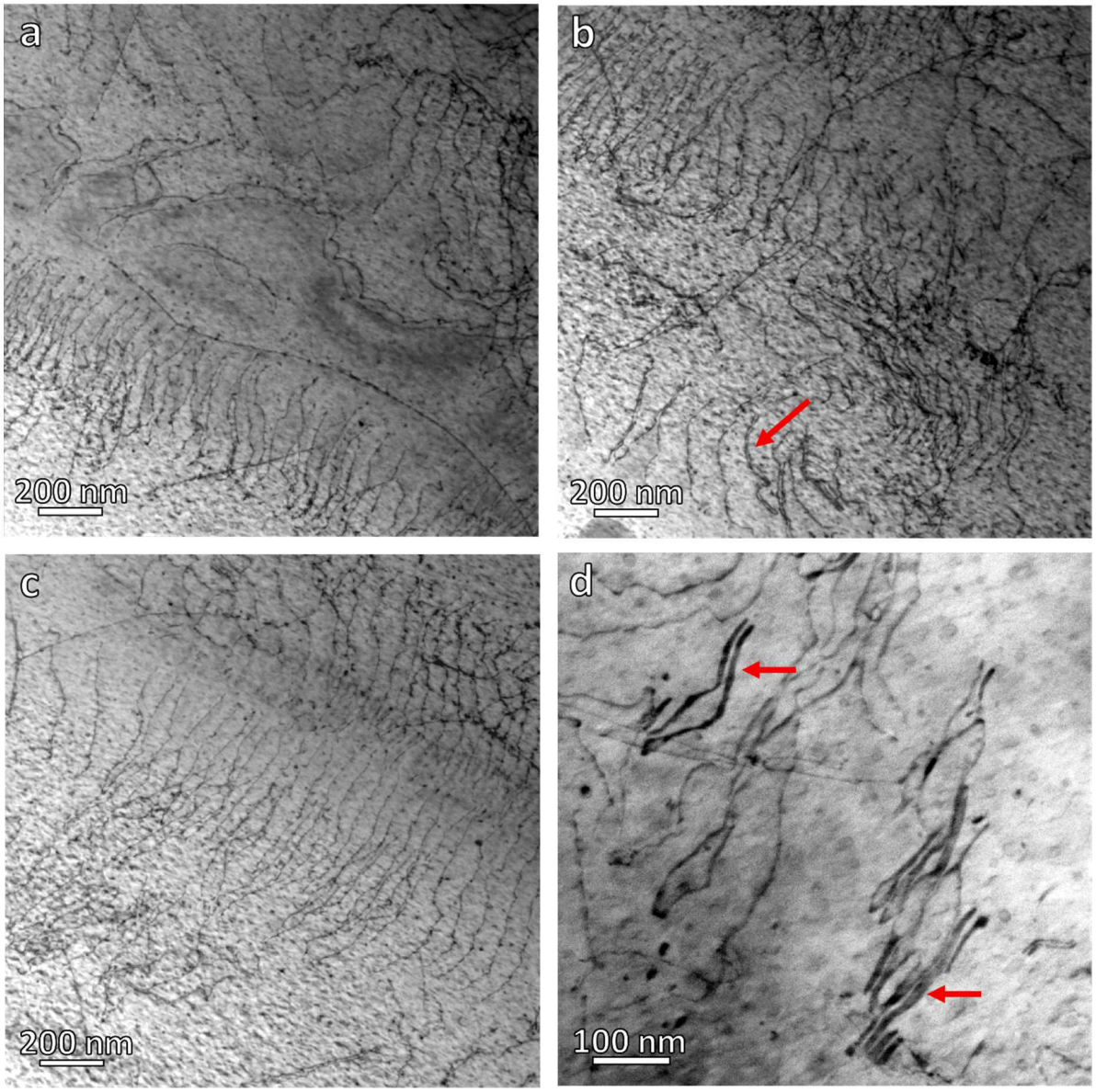

Figure 10 – Representative bright-field micrographs of the bulk slip morphology in the non-charged peak-aged specimen strained to 2% in compression. The red arrows in (b) and (d) indicate evidence of coupled dislocation pairs.

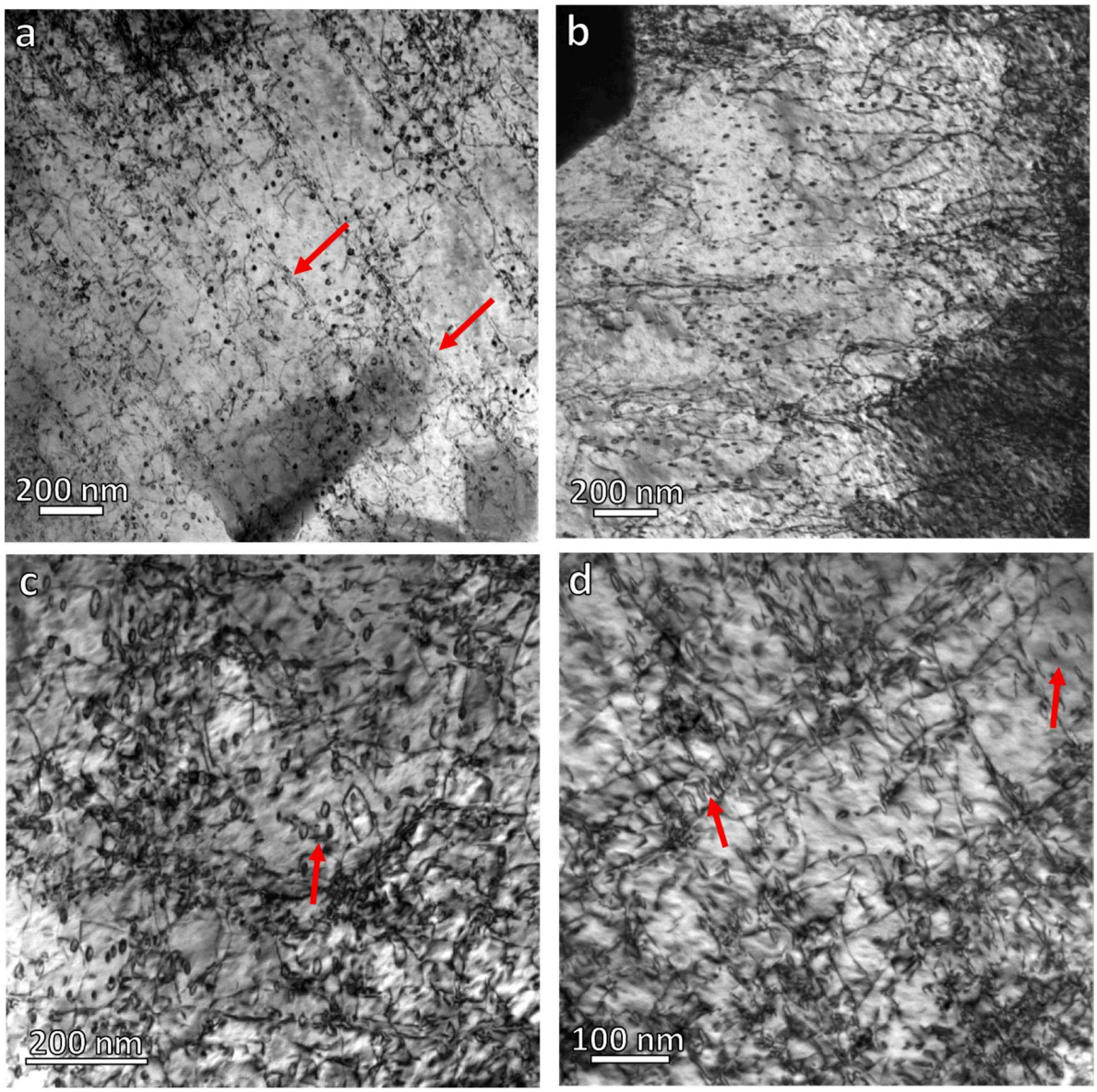

Figure 11 – Representative bright-field micrographs of the bulk slip morphology in the hydrogen-charged peak-aged specimens strained to failure. The red arrows in (a) indicate planar slip bands oriented along the trace of the {111} plane, while the red arrows in (c) and (d) denote examples of dislocation looping.

4.1.3. Effect of hydrogen on dislocation recovery (-dθ/dσ)

Figure 7b demonstrates that -dθ/dσ is increased in the presence of H for all heat treatments except the OA condition, where the non-charged and H-charged alloys exhibited a similar -dθ/dσ. While the physical basis for this 'dynamic recovery' parameter is widely debated in the literature [34–36,41,103], it is consistently related to the annihilation of dislocation line length, with larger values of -dθ/dσ implying increased rates of annihilation [34–36,42]. Moreover, unlike the θ_{max} parameter, -dθ/dσ can be unambiguously linked to the rate of dislocation annihilation (k_2) in the Kocks-Mecking model for work

hardening (Eqn. 1), as demonstrated by Cheng *et al.* in AA6111 [42]. It therefore follows that H must be increasing the rate of dislocation annihilation. Mechanistically, the two most commonly invoked pathways by which this increase in $-d\theta/d\sigma$ would be achieved are: (1) increased propensity for cross-slip or (2) easier activation of dislocation climb [34–36]. That H may act to increase the propensity for dislocation cross-slip is inconsistent with prior literature, which widely indicates that H reduces the probability of cross-slip either by stabilizing the edge component of dislocations and/or reducing the stacking fault energy [3,18–20]. That being said, the observation of loop 'stacks' in Figure 11d (one example highlighted by the left red arrow) in the PA/H alloy are consistent with an increased propensity for cross-slip, since these dislocation arrangements are commonly considered to involve multiple cross-slip steps [95,104,105]. These opposing observations are consistent with the findings of recent simulations examining the effect of H on the propensity for cross-slip in Ni [106], which illustrates the complexity of the problem and highlights that there may not be a simple answer regarding the role of cross-slip.

Considering vacancies, recent experimental and atomistic simulations agree that H lowers the vacancy formation energy, thus stabilizing an increased vacancy concentration above that expected based on thermal equilibrium in the absence of H [9,10,16,107–110]. For example, the simulations of Tanguy *et al.* indicate that the total vacancy concentration in Ni at 300 K would be increased by six orders of magnitude for the concentration of 200 wppm H observed in the current study [107]. A similar increase in expected vacancy concentration was also found by Metsue *et al.* for calculations on Ni exposed to ~100 MPa H_2 [108]. This elevated vacancy concentration may then act to increase the propensity for dislocation climb, thereby offering a potential explanation for both the observation of particle bypassing at smaller precipitate sizes and the increased rates of recovery ($-d\theta/d\sigma$) after H charging. Speculatively, it is hypothesized that the dislocation-precipitate interaction changes from the typical weak/strong-pair coupling to a mechanism that is local climb-mediated [111]. Since dislocations overcome precipitates by thermal activation [103], it is possible that while the dislocation is waiting for a successful activation event, it can interact with H-stabilized vacancies, vacancy clusters or vacancy-H complexes. This interaction is then postulated to enable the dislocation to overcome the precipitate by locally climbing over it rather than shearing or bowing around it. Critically, it has been shown that H-vacancy clusters in the glide plane will interact with dislocations leading to the formation of jog-pairs, thus facilitating the climb process as well as dipole debris formation [16]. Both of these dislocation-vacancy interactions would then explain the observed dislocation storage rate (θ_{max}) for the PA/H and OA/H conditions since they would lead to the formation of a significant amount of debris, such as that shown in Figure 11d. This hypothesis is also consistent with the observed increased recovery rate (k_2), especially in the case of the PA/H sample. As previous researchers have noted, increased recovery under conditions leading to particle bypass was

attributed to such debris annihilation reactions [42]. Finally, it is important to consider why this increased recovery rate is not observed in the H-charged OA sample. It has been shown, albeit for steady-state creep, that the climb-mediated bypass of coherent precipitates is greatly facilitated for small particles [112,113]. Thus, as the size of the precipitates increase, this climb mediated mechanism is replaced by the usual weak/strong pair coupling mechanism or Orowan looping, depending on the precipitate size.

4.2. Other possible contributions of hydrogen to dislocation-precipitate interactions

The above results indicate that H modifies dislocation-precipitate interactions, resulting in the onset of particle bypassing at smaller precipitate sizes (Figures 10-11). Based on the work hardening results presented in Figure 7, it is postulated that this transition in dislocation-precipitate interactions may be attributed to local climb enabled by H-induced increases in the equilibrium vacancy concentration. However, it is important to consider other possible intrinsic H effects that could result in the observed behavior. Specifically, the transition from particle shearing to bypassing could also be attributed to either (a) an H-induced increase in the resistance to particle shearing (*i.e.* a modification of the precipitate itself) and/or (b) a modification of the dislocation properties which would enable easier cross-slip or climb. Regarding (a), the resistance to particle shearing could be promoted by modifications in: (1) particle size (already refuted in Figure 8), (2) chemical (γ/γ' interface) strengthening, (3) stacking fault strengthening, (4) coherency strengthening *via* distinct changes in the lattice constants of the matrix and precipitate phases, (5) modulus strengthening, and (6) order strengthening [103,114–116]. It is unlikely that H segregation to the γ/γ' interface would act to increase interfacial energy [117,118]. Stacking fault strengthening occurs when the stacking fault energy (SFE) of the precipitate is much lower than the matrix [103]; however, given that the SFE is Ni_3Al is likely larger than the Ni-Cu matrix [119], such an effect can likely be neglected [46,120]. Differences from coherency strengthening can also be neglected since the stresses due to misfit strains are small (the misfit strain between γ/γ' is on the order of <0.1% for Monel K-500 [44,46,49]) and the presence of H would only reduce them further (since H has been shown to "shield" stresses [6]). Considering modulus strengthening, the shear moduli of the γ and γ' phases (assuming Ni-30Cu for γ) are quite similar, suggesting that such an effect would be negligible. Experimentalists recently suggested that hydrogen can reduce the elastic modulus in Ni [121], but these assertions are counter to atomistic modeling [122] and experiments by Hachet *et al.*, which have shown that the previously measured decreases in elastic properties with H in Ni are likely due to enhanced vacancy concentrations and vacancy clustering induced during H charging, thereby implying that H does not strongly affect elastic properties [123]. Finally, consider order hardening, which is the dominant contribution to strength in γ'-strengthened alloys [46,103]. As documented by Ardell [114], this strengthening mechanism is sensitive to variations in the antiphase boundary energy (γ_{APB}), with larger γ_{APB} values resulting in an increased resistance to shearing. Although

582 the effect of H on the γ_{APB} for Ni_3Al has not been explicitly studied, the defactant concept [124] suggests
583 that H will reduce the energy of such interfaces, which would then *increase* the propensity for particle
584 shearing [103,114,120]. In short, though the topic merits further detailed study, all of the possible means
585 by which H would increase the difficulty of shearing seem unlikely, suggesting that H-induced
586 modifications in precipitate properties are not responsible for the observed transition in behavior.

587 Considering (b), it is possible that H-induced modifications in dislocation properties could explain
588 the onset of dislocation bypassing in the PA/H alloy. Per the "defactant" concept developed by Kirchheim
589 [124] and recently considered by Sills and Cai [125], H could reduce the line energy of dislocations, thereby
590 enabling easier kink- or jog-pair nucleation required for particle bypassing by cross-slip or climb,
591 respectively. Coupled with the expected H-induced increases in the vacancy concentration [9,10,16,107–
592 110], especially if localized at the precipitate interface, this reduction in the dislocation line energy would
593 act to further ease the propensity for dislocation climb. As discussed in the preceding section, such an
594 increased ease of bypass would logically explain both the early transition from shearing to bypass, increased
595 initial hardening rates, and increased rates of recovery observed for H-charged samples in the UA and PA
596 conditions. However, detailed vetting of such synergistic influences will require further targeted modeling
597 and experimental efforts.

598 # 5. Conclusions

599 The influences of H on dislocation-precipitate interactions in a γ'-strengthened Ni-Cu superalloy were
600 systematically evaluated through mechanical testing on four isothermal heat treatments. Analysis of these
601 results, coupled with targeted transmission electron microscopy of the PA heat treatments, revealed several
602 important insights into H effects on deformation processes in precipitation-hardened alloys:

603 1. For all heat treatments, specimens pre-charged with H exhibit increased yield strength and strongly
604 reduced ductility compared to non-charged specimens.
605 2. All heat treatments exhibited a clear transition in fracture morphology from ductile, microvoid
606 coalescence to brittle, intergranular failure when pre-charged with H.
607 3. Analysis of the strain hardening behavior revealed a strong increase in θ_{max} for the H-charged
608 specimens relative to the non-charged specimens for the PA and OA conditions. An increased -
609 $d\theta/d\sigma$ was observed for the H-charged condition in the NA, UA, and PA conditions, while $-d\theta/d\sigma$
610 was unaffected by H-charging in the OA condition.
611 4. An analysis of the change in yield strength with H-charging as a function of heat treatment
612 suggested that H modifies dislocation-precipitate interactions. This postulation was confirmed by
613 TEM analysis of the deformation structure in the non-charged and H-charged PA specimens,

which showed that H induces a transition from particle shearing to bypassing at a shorter aging time.

5. While additional experiments/modeling are needed to further explore the effect of H on dislocation-precipitate interactions, it is hypothesized that the current results can be explained by a local climb-mediated bypass mechanism facilitated by H-induced increases in the equilibrium vacancy concentration.

6. Acknowledgements

The assistance of Dr. Chris San Marchi and Mr. Jeff Campbell with H charging, Mr. Michael Ritzo with TEM sample preparation and mechanical testing, as well as helpful discussions with Prof. Richard Gangloff, Prof. John Scully, Dr. Brian Somerday, Prof. Petros Sofronis, and Prof. David McDowell are all gratefully acknowledged. ZDH knowledges the support of the ALCOA Graduate Fellowship and the Volkswagen Group of North America Graduate Fellowship administered by the School of Engineering and Applied Science at the University of Virginia. SRA and JJB were supported by the Army Research Laboratory under Cooperative Agreement Number W911NF-15-2-0025. Sandia National Laboratories is a multimission laboratory managed and operated by National Technology and Engineering Solutions of Sandia, LLC., a wholly owned subsidiary of Honeywell International, Inc., for the U.S. Department of Energy's National Nuclear Security Administration under contract DE-NA-0003525. **Disclaimer:** The views and conclusions contained in this document are those of the authors and should not be interpreted as representing the official policies, either expressed or implied, of the Army Research Laboratory or the U.S. Government. The U.S. government is authorized to reproduce and distribute reprints for government purposes notwithstanding any copyright notation hereon.

7. Data Availability Statement

The raw and processed data generated during this study will be made available upon reasonable request.

8. References

[1] W.H. Johnson, On some remarkable changes produced in iron and steel by the action of hydrogen and acids, Proc. R. Soc. London. 23 (1874) 168–179. doi:10.1098/rspl.1874.0024.

[2] S.P. Lynch, Mechanisms and Kinetics of Environmentally Assisted Cracking: Current Status, Issues, and Suggestions for Further Work, Metall. Mater. Trans. A. 44A (2013) 1209–1229. doi:10.1007/s11661-012-1359-2.

[3] I.M. Robertson, P. Sofronis, A. Nagao, M.L. Martin, S. Wang, D.W. Gross, K.E. Nygren, Hydrogen Embrittlement Understood, Metall. Mater. Trans. B. (2015). doi:10.1007/s11663-015-0325-y.

[4] W.W. Gerberich, Modelling hydrogen induced damage mechanisms in metals, in: R.P. Gangloff, B.P. Somerday (Eds.), Gaseous Hydrog. Embrittlement Mater. Energy Technol., Woodhead Publishing, 2012: pp. 209–246.

[5] S.P. Lynch, Environmentally assisted cracking: Overview of evidence for an adsorption-induced localised-slip process, Acta Metall. 36 (1988) 2639–2661. doi:10.1016/0001-6160(88)90113-7.

[6] H.K. Birnbaum, P. Sofronis, Hydrogen-enhanced localized plasticity—a mechanism for hydrogen-related fracture, Mater. Sci. Eng. A. 176 (1994) 191–202. doi:10.1016/0921-5093(94)90975-X.

[7] R.A. Oriani, A Mechanistic Theory of Hydrogen Embrittlement of Steels, Berichte Der Bunsen-Gesellschaft Fur Phys. Chemie. 76 (1972) 848–857.

[8] A.R. Troiano, The Role of Hydrogen and Other Interstitials in the Mechanical Behavior of Metals: (1959 Edward De Mille Campbell Memorial Lecture), Metallogr. Microstruct. Anal. 5 (2016) 557–569. doi:10.1007/s13632-016-0319-4.

[9] M. Nagumo, Hydrogen related failure of steels – a new aspect, Mater. Sci. Technol. 20 (2004) 940–950. doi:10.1179/026708304225019687.

[10] S.K. Lawrence, Y. Yagodzinskyy, H. Hanninen, E. Korhonen, F. Tuomisto, Z.D. Harris, B.P. Somerday, Effects of grain size and deformation temperature on hydrogen-enhanced vacancy formation in Ni alloys, Acta Mater. 128 (2017) 218–226. doi:10.1016/j.actamat.2017.02.016.

[11] Z.D. Harris, S.K. Lawrence, D.L. Medlin, G. Guetard, J.T. Burns, B.P. Somerday, Elucidating the contribution of mobile hydrogen-deformation interactions to hydrogen-induced intergranular cracking in polycrystalline nickel, Acta Mater. (2018). doi:10.1016/j.actamat.2018.07.043.

[12] Y. Deng, A. Barnoush, Hydrogen embrittlement revealed via novel in situ fracture experiments using notched micro-cantilever specimens, Acta Mater. 142 (2018) 236–247. doi:10.1016/j.actamat.2017.09.057.

[13] S. Wang, A. Nagao, K. Edalati, Z. Horita, I.M. Robertson, Influence of hydrogen on dislocation self-organization in Ni, Acta Mater. 135 (2017) 96–102. doi:10.1016/j.actamat.2017.05.073.

[14] M.L. Martin, M. Dadfarnia, A. Nagao, S. Wang, P. Sofronis, Enumeration of the hydrogen-enhanced localized plasticity mechanism for hydrogen embrittlement in structural materials, Acta Mater. 165 (2019) 734–750. doi:10.1016/j.actamat.2018.12.014.

[15] M. Nagumo, K. Takai, The predominant role of strain-induced vacancies in hydrogen embrittlement of steels: Overview, Acta Mater. 165 (2019) 722–733. doi:10.1016/j.actamat.2018.12.013.

[16] A. Tehranchi, W.A. Curtin, The role of atomistic simulations in probing hydrogen effects on plasticity and embrittlement in metals, Eng. Fract. Mech. (2019). doi:10.1016/j.engfracmech.2019.106502.

[17] C.D. Beachem, A new model for hydrogen-assisted cracking (hydrogen “embrittlement”), Metall. Trans. 3 (1972) 441–455. doi:10.1007/BF02642048.

[18] P.J. Ferreira, I.M. Robertson, H.K. Birnbaum, Hydrogen effects on the interaction between dislocations, Acta Mater. 46 (1998) 1749–1757. doi:10.1016/S1359-6454(97)00349-2.

[19] I.M. Robertson, The effect of hydrogen on dislocation dynamics, Eng. Fract. Mech. 65 (2001)

671–692.

[20] D. Delafosse, Hydrogen effects on the plasticity of face centred cubic (fcc) crystals, in: R.P. Gangloff, B.P. Somerday (Eds.), Gaseous Hydrog. Embrittlement Mater. Energy Technol., Woodhead Publishing, 2012.

[21] A. Barnoush, H. Vehoff, Recent developments in the study of hydrogen embrittlement: Hydrogen effect on dislocation nucleation, Acta Mater. 58 (2010) 5274–5285. doi:10.1016/j.actamat.2010.05.057.

[22] E. Tal-Gutelmacher, R. Gemma, C.A. Volkert, R. Kirchheim, Hydrogen effect on dislocation nucleation in a vanadium (1 0 0) single crystal as observed during nanoindentation, Scr. Mater. 63 (2010) 1032–1035. doi:10.1016/j.scriptamat.2010.07.039.

[23] K.A. Nibur, D.F. Bahr, B.P. Somerday, Hydrogen effects on dislocation activity in austenitic stainless steel, Acta Mater. 54 (2006) 2677–2684. doi:10.1016/j.actamat.2006.02.007.

[24] Y.Z. Chen, H.P. Barth, M. Deutges, C. Borchers, F. Liu, R. Kirchheim, Increase in dislocation density in cold-deformed Pd using H as a temporary alloying addition, Scr. Mater. 68 (2013) 743–746. doi:10.1016/j.scriptamat.2013.01.005.

[25] Y.Z. Chen, X.Y. Ma, X.H. Shi, T. Suo, C. Borchers, K.H. Zhang, F. Liu, R. Kirchheim, Hardening effects in plastically deformed Pd with the addition of H, Scr. Mater. 98 (2015) 48–51. doi:10.1016/j.scriptamat.2014.11.012.

[26] L. Balogh, L. Capolungo, C.N. Tomé, On the measure of dislocation densities from diffraction line profiles: A comparison with discrete dislocation methods, Acta Mater. 60 (2012) 1467–1477. doi:10.1016/j.actamat.2011.10.037.

[27] A.M. Brass, D. Roux, J. Chêne, Role of secondary γ′ precipitation and of hydrogen in the first stage of the plastic deformation of the υ matrix of a Ni base superalloy single crystal, Mater. Sci. Eng. A. 323 (2002) 97–102. doi:10.1016/S0921-5093(01)01349-1.

[28] Z. Guo, M. Zhao, C. Li, S. Chen, L. Rong, Mechanism of hydrogen embrittlement in a gamma-prime phase strengthened Fe-Ni based austenitic alloy, Mater. Sci. Eng. A. 555 (2012) 77–84. doi:10.1016/j.msea.2012.06.036.

[29] A.W. Thompson, I.M. Bernstein, The Role Of Metallurgical Variables In Hydrogen-Assisted Environmental Fracture, Adv. Corros. Sci. Technol. (1980) 53–175. doi:10.1007/978-1-4615-9065-1_2.

[30] I.M. Robertson, H.K. Birnbaum, Effect of hydrogen on the dislocation structure of deformed nickel, Scr. Metall. 18 (1984) 269–274. doi:10.1016/0036-9748(84)90521-0.

[31] W.A. McInteer, A.W. Thompson, I.M. Bernstein, The effect of hydrogen on the slip character of nickel, Acta Metall. 28 (1980) 887–894. doi:10.1007/BF02655107.

[32] J.A. Wert, X. Huang, G. Winther, W. Pantleon, H.F. Poulsen, Revealing deformation microstructures, Mater. Today. 10 (2007) 24–32. doi:10.1016/S1369-7021(07)70206-7.

[33] J. Jiang, T. Ben Britton, A.J. Wilkinson, The orientation and strain dependence of dislocation structure evolution in monotonically deformed polycrystalline copper, Int. J. Plast. 69 (2015) 102–117. doi:10.1016/j.ijplas.2015.02.005.

[34] U.F. Kocks, H. Mecking, Physics and phenomenology of strain hardening: The FCC case, Prog. Mater. Sci. 48 (2003) 171–273. doi:10.1016/S0079-6425(02)00003-8.

[35] Y. Estrin, Dislocation-Density-Related Constitutive Modeling, in: A.S. Krausz, K. Krausz (Eds.), Unified Const. Laws Plast. Deform., Academic Press, 1996: pp. 69–107.

[36] E. Nes, Modelling of work hardening and stress saturation in FCC metals, Prog. Mater. Sci. 41 (1997) 129–193. doi:10.1016/S0079-6425(97)00032-7.

[37] C. Keller, E. Hug, Kocks-Mecking analysis of the size effects on the mechanical behavior of nickel polycrystals, Int. J. Plast. 98 (2017) 106–122. doi:10.1016/j.ijplas.2017.07.003.

[38] Y. Estrin, L.P. Kubin, Local strain hardening and nonuniformity of plastic deformation, Acta Metall. 34 (1986) 2455–2464.

[39] J. Christopher, B.K. Choudhary, Kinetics of Uniaxial Tensile Flow and Work Hardening Behavior of Type 316L(N) Austenitic Stainless Steel in the Framework of Two-Internal-Variable Approach, Metall. Mater. Trans. A Phys. Metall. Mater. Sci. 46 (2015) 674–687. doi:10.1007/s11661-014-2660-z.

[40] F. Barlat, M.V. Glazov, J.C. Brem, D.J. Lege, A simple model for dislocation behavior, strain and strain rate hardening evolution in deforming aluminum alloys, Int. J. Plast. 18 (2002) 919–939. doi:10.1016/S0749-6419(01)00015-8.

[41] D. Kuhlmann-Wilsdorf, Theory of plastic deformation: - properties of low energy dislocation structures, Mater. Sci. Eng. A. 113 (1989) 1–41. doi:10.1016/0921-5093(89)90290-6.

[42] L.M. Cheng, W.J. Poole, J.D. Embury, D.J. Lloyd, The influence of precipitation on the work-hardening behavior of the aluminum alloys AA6111 and AA7030, Metall. Mater. Trans. A. 34 (2003) 2473–2481. doi:10.1007/s11661-003-0007-2.

[43] K.M. Bertsch, Hydrogen effects on the evolution of plastic deformation in polycrystalline nickel: a mechanism for intergranular fracture, University of Illinois at Urbana-Champaign, 2017.

[44] G.K. Dey, P. Mukhopadhyay, Precipitation in the Ni-Cu-base alloy Monel K-500, Mater. Sci. Eng. 84 (1986) 177–189. doi:10.1016/0025-5416(86)90236-3.

[45] L.E. Shoemaker, G.D. Smith, A Century of Monel Metal: 1906 – 2006, JOM. 58 (2006) 22–26.

[46] G.K. Dey, R. Tewari, P. Rao, S.L. Wadekar, P. Mukhopadhyay, Precipitation hardening in nickel-copper base alloy monel K 500, Metall. Trans. A. 24 (1993) 2709–2719. doi:10.1007/BF02659495.

[47] J.R. Davis, ed., Nickel, Cobalt, and Their Alloys: ASM Specialty Handbook, in: 2000: pp. 167–188.

[48] Å. Gustafson, Coarsening of TiC in austenitic stainless steel - Experiments and simulations in comparison, Mater. Sci. Eng. A. 287 (2000) 52–58. doi:10.1016/S0921-5093(00)00827-3.

[49] Z.D. Harris, J.T. Burns, The effect of isothermal heat treatment on hydrogen environment-assisted cracking susceptibility in Monel K-500, Mater. Sci. Eng. A. 764 (2019) 138249. doi:10.1016/j.msea.2019.138249.

[50] S. Bechtle, M. Kumar, B.P. Somerday, M.E. Launey, R.O. Ritchie, Grain-boundary engineering

markedly reduces susceptibility to intergranular hydrogen embrittlement in metallic materials, Acta Mater. 57 (2009) 4148–4157. doi:10.1016/j.actamat.2009.05.012.

[51] B.P. Somerday, J.A. Campbell, K.L. Lee, J.A. Ronevich, C. San Marchi, Enhancing safety of hydrogen containment components through materials testing under in-service conditions, Int. J. Hydrogen Energy. (2016) 4–11. doi:10.1016/j.ijhydene.2016.04.189.

[52] J. Crank, Mathematics of Diffusion, 1975. doi:10.1016/0306-4549(77)90072-X.

[53] C.S. Marchi, B.P. Somerday, S.L. Robinson, Permeability, solubility and diffusivity of hydrogen isotopes in stainless steels at high gas pressures, Int. J. Hydrogen Energy. 32 (2007) 100–116. doi:10.1016/j.ijhydene.2006.05.008.

[54] F. Jones, R. Pehlke, Solubility of hydrogen in solid Ni− Co and Ni− Cu alloys, Metall. Trans. 2 (1971). http://link.springer.com/article/10.1007/BF02814909.

[55] C. Ko, R.B. McLellan, The thermodynamics of Ni-Cu-H solid solutions, Acta Metall. Mater. 41 (1993) 2473–2476. doi:10.1016/0956-7151(93)90327-O.

[56] H. Hagi, Diffusion Coefficients of Hydrogen in Ni-Cu and Ni-Co Alloys, Trans. Japan Inst. Met. 27 (1986) 233–240. doi:10.2320/matertrans1960.27.233.

[57] D.J. Mitchell, E.M. Edge, Permeation characteristics of some iron and nickel based alloys, J. Appl. Phys. 57 (1985) 5226–5235. doi:10.1063/1.335261.

[58] Y. Sakamoto, O. Shimizu, K. Hirayama, K. Baba, The diffusivity of hydrogen in nickel-based solid solutions, J. Phys. Chem. Solids. 49 (1988) 897–903. doi:10.1016/0022-3697(88)90006-6.

[59] J. Ai, H.M. Ha, R.P. Gangloff, J.R. Scully, Hydrogen diffusion and trapping in a precipitation-hardened nickel–copper–aluminum alloy Monel K-500 (UNS N05500), Acta Mater. 61 (2013) 3186–3199. doi:10.1016/j.actamat.2013.02.007.

[60] R.P. Gangloff, H.M. Ha, J.T. Burns, J.R. Scully, Measurement and Modeling of Hydrogen Environment-Assisted Cracking in Monel K-500, Metall. Mater. Trans. A. 45 (2014) 3814–3834. doi:10.1007/s11661-014-2324-z.

[61] B.C.R. Troconis, Z.D. Harris, H. Ha, J.T. Burns, J.R. Scully, The effect of heat-to-heat variations in metallurgy and hydrogen-metal interactions on the hydrogen embrittlement of Monel K-500, Mater. Sci. Eng. A. 703 (2017) 533–550. doi:10.1016/j.msea.2017.07.019.

[62] M.I. Baskes, J.E. Angelo, N.R. Moody, SAND-94-8741C: Atomistic calculations of hydrogen interactions with Ni3Al grain boundaries and Ni/Ni3Al interfaces, 1994.

[63] D.H. Lassila, H.K. Birnbaum, The effect of diffusive hydrogen segregation on fracture of polycrystalline nickel, Acta Metall. 34 (1986) 1237–1243. doi:10.1016/0001-6160(86)90010-6.

[64] T.H. Courtney, Mechanical Behavior of Materials, 2nd ed., McGraw-Hill, 2000.

[65] ASTM Standard E647-13: Standard Test Method for Measurement of Fatigue Crack Growth Rates, (2013). doi:10.1520/E0647-13E01.2.

[66] G.A.F. Seber, C.J. Wild, Nonlinear Regression, Wiley, 1989.

[67] R.E. Reed-Hill, R. Abbaschian, Physical metallurgy principles, Van Nostrand, Princeton, 1994.

[68] J.A. Harris, R.C. Scarberry, C.D. Stephens, Effects of Hydrogen on Engineering Properties of MONEL Nickel-Copper Alloy K-500, Corrosion. 28 (1972) 57–62.

[69] K.D. Efird, Failure of Monel Ni-Cu-Al Alloy K-500 Bolts in Seawater, Mater. Perform. 24 (1985) 37–40.

[70] L.H. Wolfe, M.W. Joosten, Failures of Nickel/Copper Bolts in Subsea Applications, SPE Prod. Eng. 3 (1988) 382–386. doi:10.2118/16632-PA.

[71] Z.D. Harris, J.D. Dolph, G.L. Pioszak, B.C. Rincon Troconis, J.R. Scully, J.T. Burns, The Effect of Microstructural Variation on the Hydrogen Environment-Assisted Cracking of Monel K-500, Metall. Mater. Trans. A. 47 (2016) 3488–3510. doi:10.1007/s11661-016-3486-7.

[72] J.T. Burns, Z.D. Harris, J.D. Dolph, R.P. Gangloff, Measurement and Modeling of Hydrogen Environment Assisted Cracking in a Ni-Cu-Al-Ti Superalloy, Metall. Mater. Trans. A. 47 (2016) 990–997. doi:10.1007/s11661-015-3315-4.

[73] M.L. Martin, B.P. Somerday, R.O. Ritchie, P. Sofronis, I.M. Robertson, Hydrogen-induced intergranular failure in nickel revisited, Acta Mater. 60 (2012) 2739–2745. doi:10.1016/j.actamat.2012.01.040.

[74] Z.D. Harris, Personal communication with Warren Poole and Sean Agnew, (2017).

[75] D.G. Ulmer, C.J. Altstetter, Hydrogen-induced strain localization and failure of austenitic stainless steels at high hydrogen concentrations, Acta Metall. Mater. 39 (1991) 1237–1248. doi:Doi: 10.1016/0956-7151(91)90211-i.

[76] V. Randle, D. Horton, Grain growth phenomena in nickel, Scr. Metall. Mater. 31 (1994) 891–895. doi:10.1016/0956-716X(94)90498-7.

[77] A.W. Thompson, Yielding in nickel as a function of grain or cell size, Acta Metall. 23 (1975) 1337–1342.

[78] Z.C. Cordero, B.E. Knight, C.A. Schuh, Six decades of the Hall–Petch effect – a survey of grain-size strengthening studies on pure metals, Int. Mater. Rev. 61 (2016) 495–512. doi:10.1080/09506608.2016.1191808.

[79] K. Takeda, N. Nakada, T. Tsuchiyama, S. Takaki, Effect of Interstitial Elements on Hall–Petch Coefficient of Ferritic Iron, ISIJ Int. 48 (2008) 1122–1125. doi:10.2355/isijinternational.48.1122.

[80] S. Takaki, D. Akama, N. Nakada, T. Tsuchiyama, Effect of Grain Boundary Segregation of Interstitial Elements on Hall-Petch Coefficient in Steels, Mater. Trans. 55 (2013) 28–34. doi:10.2320/matertrans.ma201314.

[81] Y. Mine, N. Horita, Z. Horita, K. Takashima, Effect of ultrafine grain refinement on hydrogen embrittlement of metastable austenitic stainless steel, Int. J. Hydrogen Energy. 42 (2017) 15415–15425. doi:10.1016/j.ijhydene.2017.04.249.

[82] I.M. Bernstein, The effect of hydrogen on the deformation of iron, Scr. Metall. 8 (1974) 343–349. doi:10.1016/0036-9748(74)90136-7.

[83] G.R. Caskey, Effect of hydrogen on work hardening of Type 304L austenitic stainless steel, Scr. Metall. 15 (1981) 1183–1186.

[84] B.A. Wilcox, G.C. Smith, Intercrystalline fracture in hydrogen-charged nickel, Acta Metall. 13 (1965) 331–343.

[85] Y. Mishima, S. Ochiai, N. Hamao, M. Yodogawa, T. Suzuki, Solid Solution Hardening of Nickel - Role of Transition Metal and B-subgroup Solutes, Trans. Japan Inst. Met. 27 (1986) 656–664.

[86] N.F. Mott, Mechanical strength and creep in metals, in: Imperfections Nearly Perfect Cryst., 1952: pp. 173–196.

[87] M.Z. Butt, P. Feltham, Solid-solution hardening, Acta Metall. 26 (1978) 167–173.

[88] R.J. Arsenault, S. Patu, D.M. Esterling, Computer simulation of solid solution strengthening in Fcc alloys: Part I. Friedel and mott limits, Metall. Trans. A. 20 (1989) 1411–1418. doi:10.1007/bf02665498.

[89] D. Ma, M. Friák, J. Von Pezold, D. Raabe, J. Neugebauer, Computationally efficient and quantitatively accurate multiscale simulation of solid-solution strengthening by ab initio calculation, Acta Mater. 85 (2015) 53–66. doi:10.1016/j.actamat.2014.10.044.

[90] G.P.M. Leyson, L.G. Hector, W.A. Curtin, Solute strengthening from first principles and application to aluminum alloys, Acta Mater. 60 (2012) 3873–3884. doi:10.1016/j.actamat.2012.03.037.

[91] Y. Nakada, S. Keh, Solid solution strengthening in Fe-N single crystals, Acta Metall. 16 (1968) 903–914.

[92] W. Rauscher, W. Köster, RELATIONS BETWEEN THE MODULUS OF ELASTICITY OF BINARY ALLOYS AND THEIR STRUCTURE, Stuttgart, Germany, 1951.

[93] B. Baranowski, S. Majchrzak, T.B. Flanagan, The volume increase of fcc metals and alloys due to interstitial hydrogen over a wide range of hydrogen contents, J. Phys. F Met. Phys. 1 (1971) 258–261. doi:10.1088/0305-4608/1/3/307.

[94] C.G. Schmidt, A.K. Miller, The effect of solutes on the strength and strain hardening behavior of alloys, Acta Metall. 60 (1982) 615–625.

[95] J.W. Martin, Micromechanisms in particle-hardened alloys, Cambridge University Press, Cambridge, UK, 1980.

[96] J.C. Fisher, E.W. Hart, R.H. Pry, The hardening of metal crystals by precipitate particles, Acta Metall. 1 (1953) 336–339.

[97] L.M. Brown, D.R. Clarke, Work hardening due to internal stresses in composite materials, Acta Metall. 23 (1975) 821–830. doi:10.1016/0001-6160(75)90198-4.

[98] E.M. Francis, B.M.B. Grant, J.Q. Da Fonseca, P.J. Phillips, M.J. Mills, M.R. Daymond, M. Preuss, High-temperature deformation mechanisms in a polycrystalline nickel-base superalloy studied by neutron diffraction and electron microscopy, Acta Mater. 74 (2014) 18–29. doi:10.1016/j.actamat.2014.04.028.

[99] M. Preuss, J.Q. Da Fonseca, B. Grant, E. Knoche, R. Moat, M. Daymond, The effect of γ′ particle size on the deformation mechanism in an advanced polycrystalline nickel-base superalloy, in: Superalloys 2008, 2008: pp. 405–414.

[100] H.J. Stone, T.M. Holden, R.C. Reed, On the generation of microstrains during the plastic deformation of Waspaloy, Acta Mater. 47 (1999) 4435–4448. doi:10.1016/S1359-6454(99)00314-6.

[101] D.E. Kim, S.L. Shang, Z.K. Liu, Effects of alloying elements on elastic properties of Ni3Al by first-principles calculations, Intermetallics. 18 (2010) 1163–1171. doi:10.1016/j.intermet.2010.02.024.

[102] A. Bourret, Irradiation damage in nickel and iron in a high-voltage electron microscope and threshold energy determination, Phys. Status Solidi. 4 (1971) 813–825.

[103] A.S. Argon, Strengthening mechanisms in crystal plasticity, Oxford University Press, 2008.

[104] F.J. Humphreys, P.B. Hirsch, The Deformation of Single Crystals of Copper and Copper-Zinc Alloys Containing Alumina Particles. II. Microstructure and Dislocation-Particle Interactions, Proc. R. Soc. A Math. Phys. Eng. Sci. 318 (1970) 73–92. doi:10.1098/rspa.1970.0134.

[105] Y. Xiang, D.J. Srolovitz, L.T. Cheng, W. E, Level set simulations of dislocation-particle bypass mechanisms, Acta Mater. 52 (2004) 1745–1760. doi:10.1016/j.actamat.2003.12.016.

[106] Y. Tang, J.A. El-Awady, Atomistic simulations of the interactions of hydrogen with dislocations in fcc metals, Phys. Rev. B - Condens. Matter Mater. Phys. 86 (2012) 1–13. doi:10.1103/PhysRevB.86.174102.

[107] D. Tanguy, Y. Wang, D. Connétable, Stability of vacancy-hydrogen clusters in nickel from first-principles calculations, Acta Mater. 78 (2014) 135–143. doi:10.1016/j.actamat.2014.06.021.

[108] A. Metsue, A. Oudriss, X. Feaugas, Hydrogen solubility and vacancy concentration in nickel single crystals at thermal equilibrium: New insights from statistical mechanics and ab initio calculations, J. Alloys Compd. 656 (2016) 555–567. doi:10.1016/j.jallcom.2015.09.252.

[109] S. Harada, S. Yokota, Y. Ishii, Y. Shizuku, M. Kanazawa, Y. Fukai, A relation between the vacancy concentration and hydrogen concentration in the Ni-H, Co-H and Pd-H systems, J. Alloys Compd. 404–406 (2005) 247–251. doi:10.1016/j.jallcom.2005.02.077.

[110] Y. Fukai, Formation of superabundant vacancies in M-H alloys and some of its consequences: A review, J. Alloys Compd. 356–357 (2003) 263–269. doi:10.1016/S0925-8388(02)01269-0.

[111] J. Cadek, Creep in Metallic Materials, Elsevier, 1988.

[112] E.A. Marquis, D.C. Dunand, Model for creep threshold stress in precipitation-strengthened alloys with coherent particles, Scr. Mater. 47 (2002) 503–508. doi:10.1016/S1359-6462(02)00165-3.

[113] D.N. Seidman, E.A. Marquis, D.C. Dunand, Precipitation strengthening at ambient and elevated temperatures of heat-treatable Al(Sc) alloys, Acta Mater. 50 (2002) 4021–4035. doi:10.1016/S1359-6454(02)00201-X.

[114] A.J. Ardell, Precipitation hardening, Metall. Trans. A. 16 (1985) 2131–2165. doi:10.1007/BF02670416.

[115] T. Gladman, Precipitation hardening in metals, Mater. Sci. Technol. 15 (2004) 30–36. doi:10.1179/026708399773002782.

[116] A. Kelly, R.B. Nicholson, Precipitation hardening, Prog. Mater. Sci. 10 (1963) 151–391.

[117] S. Jothi, T.N. Croft, S.G.R. Brown, Influence of grain boundary misorientation on hydrogen embrittlement in bi-crystal nickel, Int. J. Hydrogen Energy. (n.d.). doi:http://dx.doi.org/10.1016/j.ijhydene.2014.07.020.

[118] A. Alvaro, I. Thue Jensen, N. Kheradmand, O.M. Løvvik, V. Olden, Hydrogen embrittlement in nickel, visited by first principles modeling, cohesive zone simulation and nanomechanical testing, Int. J. Hydrogen Energy. 40 (2015) 16892–16900. doi:10.1016/j.ijhydene.2015.06.069.

[119] Y.F. Wen, J. Sun, J. Huang, First - Principles study of stacking fault energies in Ni3Al intermetallic alloys, Trans. Nonferrous Met. Soc. China (English Ed. 22 (2012) 661–664. doi:10.1016/S1003-6326(11)61229-6.

[120] D. Raynor, J.M. Silcock, Strengthening Mechanisms in γ′ Precipitating Alloys, Met. Sci. 4 (1970) 121–130. doi:10.1179/msc.1970.4.1.121.

[121] S.K. Lawrence, B.P. Somerday, M.D. Ingraham, D.F. Bahr, Probing the Effect of Hydrogen on Elastic Properties and Plastic Deformation in Nickel Using Nanoindentation and Ultrasonic Methods, Jom. 70 (2018) 1068–1073. doi:10.1007/s11837-018-2850-z.

[122] M. Wen, A. Barnoush, K. Yokogawa, Calculation of all cubic single-crystal elastic constants from single atomistic simulation: Hydrogen effect and elastic constants of nickel, Comput. Phys. Commun. 182 (2011) 1621–1625. doi:10.1016/j.cpc.2011.04.009.

[123] G. Hachet, A. Metsue, A. Oudriss, X. Feaugas, Influence of hydrogen on the elastic properties of nickel single crystal: A numerical and experimental investigation, Acta Mater. 148 (2018) 280–288. doi:10.1016/j.actamat.2018.01.056.

[124] R. Kirchheim, Reducing grain boundary, dislocation line and vacancy formation energies by solute segregation. I. Theoretical background, Acta Mater. 55 (2007) 5129–5138. doi:10.1016/j.actamat.2007.05.047.

[125] R.B. Sills, W. Cai, Free energy change of a dislocation due to a Cottrell atmosphere, Philos. Mag. 98 (2018) 1491–1510. doi:10.1080/14786435.2018.1441560.